



**HAL**  
open science

## High-P metamorphism in the Mesoproterozoic: petrochronological insights from the Grenville Province

Caroline Lotout, Aphrodite Indares, Jeffrey Vervoort, Etienne Deloule

### ► To cite this version:

Caroline Lotout, Aphrodite Indares, Jeffrey Vervoort, Etienne Deloule. High-P metamorphism in the Mesoproterozoic: petrochronological insights from the Grenville Province. *Precambrian Research*, 2023, 399, pp.107208. 10.1016/j.precamres.2023.107208 . hal-04323129

**HAL Id: hal-04323129**

**<https://hal.science/hal-04323129>**

Submitted on 5 Dec 2023

**HAL** is a multi-disciplinary open access archive for the deposit and dissemination of scientific research documents, whether they are published or not. The documents may come from teaching and research institutions in France or abroad, or from public or private research centers.

L'archive ouverte pluridisciplinaire **HAL**, est destinée au dépôt et à la diffusion de documents scientifiques de niveau recherche, publiés ou non, émanant des établissements d'enseignement et de recherche français ou étrangers, des laboratoires publics ou privés.

1 **High-*P* metamorphism in the Mesoproterozoic: petrochronological insights**  
2 **from the Grenville Province**

3

4

5 Caroline Lotout<sup>1,2</sup>, Aphrodite Indares<sup>2</sup>, Jeffrey Vervoort<sup>3</sup>, Etienne Deloule<sup>1</sup>

6

7 <sup>1</sup> Université de Lorraine, CNRS, CRPG, F-54000 Nancy, France

8 <sup>2</sup> Department of Earth Sciences, Memorial University of Newfoundland, St. John's, Canada

9 <sup>3</sup> School of the Environment, Washington State University, United States

10

11 Corresponding author: Caroline Lotout, [caroline.lotout@uca.fr](mailto:caroline.lotout@uca.fr)

12

13

14

15

16

17

18

19

20

21

22

23 **Abstract:**

24 In the Grenville Province, high-P rocks that are discontinuously exposed along the margin of  
25 the allochthonous belt preserve the record of deep crustal processes and are an essential  
26 puzzle piece to understanding Mesoproterozoic geodynamics. The Manicouagan Imbricate  
27 zone (MIZ) is one of the three high-P domains from the Grenville Province. It is located in the  
28 Central Grenville between the Parautochthonous Belt to the North and the orogenic hinterland  
29 to the South, that were metamorphosed during the 1005–980 Ma Rigolet and 1080–1020 Ma  
30 Ottawa orogenic phases, respectively. In the western MIZ, the Lelukuau Terrane (LT)  
31 mostly consists of Labradorian-age (~1650 Ma) mafic suites with a fringe of aluminous rocks  
32 at its southern edge. Metamafic samples from the Western and Eastern parts of the MIZ  
33 display a peak assemblage of garnet, clinopyroxene, plagioclase, rare pargasite or edenite, and  
34 quartz ± kyanite. Pseudosection modelling suggests high-P granulite peak conditions at ca. 14  
35 to 16 kbar and 800–900°C, with the scarcity of hydrous phases and quartz explaining the lack  
36 of evidence for partial melting. Zircon cores from the Western LT sample show a maximum  
37 magmatic age of ca 1.6 Ga. Lu–Hf and Sm–Nd dating on garnet from this sample yield ages  
38 of  $1020 \pm 7$  Ma and  $1005 \pm 13$  Ma, respectively, overlapping within error and inferred to  
39 represent peak metamorphic conditions followed by fast cooling. In the Eastern LT sample,  
40 garnet Lu–Hf dating yields two ages that are consistent with a petrographically preserved two  
41 stage growth, at  $1033 \pm 6$  Ma and  $1013 \pm 6$  Ma, while the Sm–Nd age indicates cooling at  
42  $1003 \pm 8$  Ma. The recorded high-P granulite facies conditions highlight a late Ottawa to  
43 Rigolet-age localized crustal thickening at the margin of the hinterland during the propagation  
44 of the orogen to the NW, with a possible younging of the high-P granulite-facies  
45 metamorphism from the Eastern to Western LT. These new results indicate that the high-P  
46 belt in the Central Grenville does not represent the exhumed base of an Ottawa age orogenic  
47 plateau, as previously proposed, and that no tectonic hiatus exists between the two orogenic

48 phases, as generally thought. Finally, this publication highlights the diversity and  
49 diachronicity of the high-P domains in the Grenville Province.

50

51 **Keywords:** Garnet geochronology, Zircon geochronology, high-P granulite, Grenville  
52 Orogeny, Mesoproterozoic

## 53 **1. Introduction**

54 High-pressure (high-P) rocks, namely eclogite, high-P granulite, and kyanite-bearing  
55 migmatite provide important evidence for active plate tectonics, recording the burial of the  
56 crust and crustal thickening in convergence zones. In those settings, timescales and conditions  
57 of metamorphism are crucial in deciphering the evolution of the lithosphere, as the tectonic  
58 scenarios invoked largely rely on the rates of burial and exhumation of metamorphic terranes  
59 (e.g., Warren, 2013), their corresponding size, and their temporal and spatial distribution  
60 within an orogen (e.g., Kylander-Clark et al., 2012). In this regard, the advent of  
61 petrochronology (see RIMG 2017 special volume, Kohn et al., 2017) has provided valuable  
62 insights on the petrological evolution of chronometers by integrating their textural, isotopic,  
63 and elemental context. Zircon and monazite are often targeted to access time information  
64 during metamorphism (e.g., Baldwin and Brown, 2008; Gasser et al., 2012; Štípská et al.,  
65 2016; Wang et al., 2017), as their potential equilibrium with garnet can be assessed by their  
66 trace element record (e.g., Rubatto, 2002, 2017; Whitehouse and Platt, 2003). In recent years,  
67 an increasing number of publications have highlighted the need to combine multiple  
68 petrochronological tools in high-grade terranes (e.g., Manzotti et al., 2018; Lotout et al., 2018,  
69 2020; Wang et al., 2019; Du et al., 2021; Li et al., 2022). This is supported by the fact that  
70 prograde and/or retrograde metamorphic overprints can result in a complex record of  
71 accessory minerals reflecting lack of equilibrium at the rock scale, and incomplete U–Pb  
72 resetting or trace element inheritance (e.g., Harley et al., 2007; Yakymchuk and Brown, 2014;  
73 Whitehouse et al., 2014; Kohn et al., 2015; Taylor et al., 2016; Lotout, et al., 2018; Pitra et al.,  
74 2022), thus making it difficult to link ages to specific P–T stages. Petrochronological  
75 investigation of both rock-forming minerals (like garnet) and accessory minerals (like zircon)  
76 provides a strategy to obtain significant timing information. Combined with P–T

77 thermodynamic modelling, this has proven to be one of the most reliable approaches to  
78 decipher the style of tectonic processes.

79 Exhumed cores of ancient orogens give direct access to formerly deep and hot levels of the  
80 crust offering opportunities to both assess the condition and duration of high-T and high-P  
81 processes and investigate the tectonic evolution of orogenic roots. The Grenville Province,  
82 exposed in eastern North America from Canada to the Adirondack Mountains of the United  
83 States (Fig. 1a), is recognized as the first Large Hot Orogen (LHO) on Earth (Rivers, 2009),  
84 and is attributed to the collision between Laurentia and Amazonia in the late  
85 Mesoproterozoic. Its orogenic core (Allochthonous belt, or hinterland) is an assembly of  
86 crustal segments that were metamorphosed, mostly at granulite-facies conditions, at different  
87 depths during the 1090–1020 Ma Ottawan phase of the Grenvillian orogeny (Fig. 1b) and is  
88 inferred to represent remnants of a collapsed orogenic plateau (Rivers, 2008; 2012). In  
89 contrast, the Parautochthonous belt of the Grenville Province (Fig. 1b) was deformed and  
90 metamorphosed later, during the final propagation of the orogen to the NNW (Rigolet Phase;  
91 1005–980 Ma), and after a presumed tectonometamorphic hiatus of about 15 Myr (e.g.,  
92 Rivers, 2009, 2012).

93 Although geodynamic modelling has addressed key tectonic features of the Grenville orogen  
94 (e.g., Jamieson et al., 2007, 2010), metamorphic data, crucial for tectonic interpretations, are  
95 patchy and incomplete (see Indares and Dunning, 2018, and Indares, 2020 for a review), and  
96 petrochronological studies remain scarce. For instance, garnet ages are only reported from  
97 mid-P and high-T rocks from the Virginia Blue Ridge area (Johnson et al., 2018, 2020), a  
98 tectonic window within the Appalachian Orogen.

99 In addition, recent debate on Mesoproterozoic global tectonic regimes, and changes of  
100 orogenic style with time, has been spirited (e.g., Cawood and Hawkesworth, 2014; Tang et al.,  
101 2021; Roberts et al., 2022), and some aspects of the orogen are questioned by recent studies.

102 For instance, Spencer et al. (2021), made the case that the orogenic crust was thin in the  
103 Mesoproterozoic and Brudner et al., (2022) disputed the existence of a long-lived highly  
104 elevated orogenic plateau in the Grenville. Considering this, high-P rocks exposed in the  
105 Grenville Province are essential pieces to the Mesoproterozoic geodynamic puzzle as they  
106 record orogenic processes operating at depth. These rocks are documented on either side of  
107 the Allochthon Boundary Thrust (Fig. 1b). In the hinterland, they are grouped within the  
108 “high-P belt” (Rivers et al., 2002) and occur (i) as mafic pods of eclogite retrogressed to  
109 granulite, with early Ottawaan metamorphic ages, dispersed in orthogneiss (e.g.,  
110 Davidson 1990; Marsh & Culshaw, 2014; western Grenville), and (ii) in coherent lithotectonic  
111 packages dominated by mafic rocks with well-preserved high-P granulite to eclogite facies  
112 assemblages (Indares 1997, Indares et al., 1998, 2000; central Grenville). In addition,  
113 eclogitized metagabbros are reported in the Parautochthonous Molson Lake terrane (Indares  
114 1993; Indares and Rivers 1995).

115 This contribution focuses on high-P mafic rocks from the Manicouagan Imbricate zone (MIZ)  
116 of the Central Grenville. The MIZ is located structurally below the mid-P belt of the  
117 hinterland, (Fig. 1b, c) and based on this configuration is well suited for comparing processes  
118 operating in deep to intermediate levels of the Ottawaan orogenic crust. Based on poorly  
119 constrained Ottawaan ages reported in the early literature (Indares et al., 2000), the MIZ was  
120 inferred to represent the extruded base of the thickened Ottawaan crust (Rivers 2008), and  
121 therefore it is a key area to bring new fundamental constraints on the timing and duration of  
122 high-P metamorphism and subsequent tectonic evolution.

123 The samples were collected in the early 90s in the context of the Lithoprobe project (see  
124 Clowes et al., 1999; Rivers et al., 2012). In the context of the present study, they were  
125 investigated using textural observation, P–T thermodynamic modelling, garnet Lu–Hf and  
126 Sm–Nd dating, zircon U–Pb dating, and trace element analysis in garnet and zircon. This

127 study shows that the high-P rocks of the Central Grenville experienced peak high-P  
128 metamorphism straddling the interval between the Ottawa and Rigolet phases and reveals a  
129 continuum where a tectonometamorphic hiatus was previously inferred. It also highlights that  
130 this high-P granulite metamorphism reflects localized crustal thickening at the margin of the  
131 hinterland, as the orogen was progressing towards the Grenville front. By bringing new P–T–t  
132 information on this high-P metamorphic event of the Grenville Orogen, this study also  
133 highlights the tectonically active character of the lithosphere during Mesoproterozoic times.

134

## 135 2. Geological background

136 The MIZ is a 2000 km<sup>2</sup> area of stacked high-P crustal slices (e.g., Indares, 1997), located in  
137 the central Grenville between the structurally lower Parautochthonous Gagnon terrane to the  
138 north, and structurally higher lithotectonic units of the hinterland, to the south (Fig. 1b, c).

139 The Gagnon terrane consists of Archean basement and Paleoproterozoic cover  
140 metamorphosed, in the vicinity of the MIZ, at amphibolite to high-P granulite facies  
141 conditions at ~990 to 980 Ma (Jordan et al. 2006; Jannin et al., 2018a). South of the MIZ, the  
142 mid-P belt of the hinterland consists of ~1.5–1.4 and 1.2 Ga plutonic and supracrustal rocks  
143 metamorphosed under mid-P granulite-facies conditions between 1.08 and 1.04 Ga (Dunning  
144 and Indares 2010; Lasalle et al. 2014). However, its contact with the MIZ is obscured by the  
145 Triassic Manicouagan impact crater. In contrast, to the SE, the MIZ is in direct contact with  
146 the Hart Jaune terrane, which represents the highest crustal levels of the hinterland in this area  
147 that largely escaped Grenvillian-age metamorphism and deformation (part of the Orogenic  
148 Lid; Rivers 2008).

149 The MIZ is subdivided into two terranes, Lelukuau (LT, lower unit) and Tshenukutish (TT,  
150 upper unit; Fig. 1c). Both terranes are dominated by plutonic units, with a discontinuous

151 fringe of supracrustal rocks, including anatectic aluminous gneisses, exposed in the southern  
152 MIZ along the shores of the Manicouagan reservoir (Indares and Dunning 2001, Dunning and  
153 Indares, 2010).

154 The LT is the largest component of MIZ and is mostly composed of Labradorian-age  
155 anorthosite–mangerite–charnockite–granite (AMCG) bodies emplaced at 1650–1630 Ma  
156 (Indares et al., 1998). In the eastern MIZ, the structurally higher TT is an assembly of highly  
157 deformed tectonic slices, composed of Labradorian-age AMCG, Pinwarian-age granites  
158 emplaced at ca. 1450 Ma, and ca. 1190 Ma mafic sills (Cox and Indares, 1999; Indares et al.,  
159 2000). Mafic rocks in the two terranes show different metamorphic textures. Coronitic or  
160 granoblastic textures, based on the protolith type (sill vs other types of magmatic bodies), are  
161 observed in the TT (Indares, 2003; Cox and Indares, 1999), while mafic rocks from the LT are  
162 pervasively recrystallized in a granoblastic assemblage of garnet–clinopyroxene–  
163 plagioclase ± amphibole ± quartz, up to the point that the magmatic archive is only deduced  
164 from the presence of microdomains mimicking igneous textures (Indares, 2003). P–T  
165 estimates are mostly restricted to traditional thermobarometry results, with P–T conditions in  
166 the range of 14–18 kbar and 800–900°C in the LT (Indares, 1997, 2003; Indares and Dunning,  
167 2004), and 780–930°C and 16–19 kbar in the TT (Cox and Indares, 1999). The P–T  
168 conditions of the LT are consistent with results of subsequent pseudosection modelling (Yang  
169 and Indares, 2005). This was, however, limited by the lack of thermodynamic melt data suited  
170 for mafic compositions, only recently provided by Green et al. (2016), to appropriately  
171 bracket the temperature range. Metamorphic ages on mafic rocks, that represent the main rock  
172 types of the MIZ, are scarce and mostly restricted to lower intercepts obtained by single  
173 zircon grain dissolution using ID-TIMS, at  $1052 \pm 19$  Ma (Indares et al., 1998), and  
174  $1030 \pm 12$  Ma (Cox et al., 1998; Fig. 2). The best approximation for the age of high-P  
175 metamorphism is provided by a set of syn-orogenic dykes (“Themines dykes”; Indares and

176 Dunning 2004) cropping out in southern MIZ, which display high-P granuloblastic assemblages  
177 (garnet–clinopyroxene–plagioclase–quartz) and are interpreted to have been emplaced at  
178 high-P conditions. One of these dykes, in the TT, was dated at  $1039 \pm 2$  Ma (Indares et al.,  
179 1998).

180 The high-P anatectic aluminous rocks exposed in the southern MIZ have kyanite–garnet–K-  
181 feldspar–plagioclase–quartz  $\pm$  biotite assemblages, with textures consistent with peak and  
182 melt crystallization P–T conditions in the kyanite stability field. Pseudosection modelling has  
183 constrained the peak P–T conditions at 15–16 kbar and 875°C (Indares et al., 2008; Lasalle  
184 and Indares, 2014; Kendrick and Indares, 2018). In the southern LT, monazite from one  
185 sample was analyzed by both ID-TIMS on single grains (Dunning and Indares, 2010) and  
186 later by *in situ* Laser Ablation Inductively Coupled Plasma Mass Spectrometry (LA-ICPMS)  
187 (Lasalle et al., 2014). Both methods yielded complex age data and the age of Grenvillian  
188 metamorphism remains difficult to interpret owing to strong inheritance. LA-ICPMS ages  
189 spread from  $1362 \pm 26$  Ma to  $1025 \pm 22$  Ma, with a cluster at 1070–1050 Ma, and a poorly  
190 supported weighted average age of  $1061 \pm 9.6$  Ma while ID-TIMS data yielded an average  
191 age for Grenvillian metamorphism at  $1044 \pm 1.5$  Ma. These data are interpreted to reflect  
192 protracted growth of monazite during anatexis, and, in the case of ID-TIMS, varied mixing of  
193 distinct monazite age domains (Lasalle et al., 2014). In contrast, monazite ages obtained in 5  
194 samples from the southern boundary of the TT (single-grain dissolution, ID-TIMS, Indares  
195 and Dunning, 2001) are better constrained as they are tightly clustered at the sample scale,  
196 ranging from  $1040 \pm 2$  Ma to  $1017 \pm 2$  Ma from West to East (Fig. 2). These late Ottawa  
197 ages likely indicate diachronism of the metamorphism, however they only represent the  
198 southern fringe of the MIZ, while the timing of the high-P metamorphism in the interior of the  
199 MIZ, that is dominated by mafic rocks, remains poorly constrained.

200

### 201 **3. Analytical Methods**

202 The analytical techniques were carried out at the Core Research Equipment and Instrument  
203 Training (CREAIT) Network at Memorial University of Newfoundland (MUN, St John's,  
204 Canada), Centre de Recherches Petrographiques et Géochimiques (CRPG, Nancy, France),  
205 and Radiogenic and Isotopic Geochronology Lab (RIGL, Washington State University,  
206 Pullman, USA). All operating conditions, standards, chemical procedures, and solid solution  
207 models used and carried out are described in detail in the Appendix.

208 Bulk rock powders were produced at MUN and major and trace elements analyses were  
209 performed by Inductively Coupled Plasma Atomic Emission Spectrometry (ICP-AES) and  
210 Inductively Coupled Plasma Mass Spectrometry (ICPMS), respectively, at the SARM  
211 laboratory of CRPG, following the procedure described in Carignan et al. (2001;  
212 Supplementary Table 1). Thin sections were imaged by Scanning Electron Microscope (SEM)  
213 equipped with Mineral Liberation Analysis (MLA) software to provide false color mineral  
214 maps illustrating textures, X-Ray maps of garnet were obtained using an Electron Probe  
215 Microanalyzer (EPMA), and zircon were imaged using a SEM equipped with a Deben  
216 Centaurus CathodoLuminescence (CL) detector at CREAIT (MUN). Quantitative mineral  
217 analyses for major elements were carried out using a EPMA (Supplementary Table 2) and  
218 trace elements in garnet were measured by LA-ICPMS (Supplementary Table 3) at CREAIT  
219 (MUN). P–T pseudosections have been calculated in the  $\text{Na}_2\text{O}-\text{CaO}-\text{FeO}-\text{MgO}-\text{Al}_2\text{O}_3-$   
220  $\text{SiO}_2-\text{H}_2\text{O}-\text{Fe}_2\text{O}_3$  (NCFMASHO) system using the software Theriak/Domino (de Capitani  
221 and Petrakakis, 2010), and the internally consistent thermodynamic data set 6.2 (Holland and  
222 Powell, 2011, update ds62, 6th February 2012). Garnet and zircon mineral separation was  
223 performed at MUN following standard procedure to concentrate heavy minerals and picking.  
224 Lu-Hf and Sm-Nd garnet dating was performed at RIGL, following procedures described in  
225 Cheng et al., (2008) and Johnson et al., (2018). Isotope data and corresponding calculated

226 dates were produced using isoplot (Ludwig, 2003) and ages are reported at 95% confidence  
 227 level (Table 2, Fig. 9.). U-Pb and REE analyzes in zircon were performed at the National Ion  
 228 Probe facility hosted by the CRPG, following Deloule et al. (2002) and Jeon & Whitehouse  
 229 (2014). Isotope data are reported in Supplementary Table 3 and corresponding calculated  
 230 dates, produced using isoplot (Ludwig, 2003), are shown in Fig.10 and reported at 95%  
 231 confidence level. Abbreviations used in this manuscript are: apfu = atom per formula unit; g =  
 232 garnet; cpx = clinopyroxene; di = diopside; amp = amphibole; prg = pargasite; edn = edenite;  
 233 mu = muscovite; pl = plagioclase; scp = scapolite; q = quartz; ru = rutile; bi = biotite; ky =  
 234 kyanite; zrn = zircon; ap = apatite; liq = liquid. Other symbols used (mole/atomic proportion)  
 235 are:  $X_{alm} = Fe / (Ca + Fe + Mg + Mn)$ ;  $X_{py} = Mg / (Ca + Fe + Mg + Mn)$ ;  $X_{grs} = Ca / (Ca + Fe +$   
 236  $Mg + Mn)$ ;  $X_{sps} = Mn / (Ca + Fe + Mg + Mn)$  (garnet);  $X_{Jd} = Na / (Na + Ca)$ ;  $CaT = Al^{IV} - X_{Jd}$   
 237 (cpx);  $X_{Mg} = Mg / (Fe + Mg)$  (garnet, clinopyroxene, amphibole);  $X_{An} = Ca / (Ca + Na + K)$ ;  
 238  $X_{Ab} = Na / (Ca + Na + K)$  (plagioclase);  $X_{CO3} = CO3 / (CO3 + SO4 + Cl)$ ;  $X_{eqAn} = 100 (Al -$   
 239  $3) / 3$ ;  $X_{Me} = Ca / (Ca + Na)$  (scapolite);  $Mg\# = 100 * Mg / (Mg + Fe)$  (bulk rock).

240

## 241 **4. Results**

### 242 **4.1. Sample description**

243 Three mafic rocks were selected for this study. They belong to distinct levels of the LT  
 244 following Indares (1997) and all have a gabbroic composition with high  $Al_2O_3$  content (17 to  
 245 20 wt%) and Mg# ranging from 41.7 to 61.7% (Supplementary Table 1). All samples are  
 246 pervasively recrystallized showing a medium to fine grained granoblastic texture and  
 247 containing the mineral assemblage garnet–clinopyroxene–plagioclase–amphibole–scapolite  
 248 with varied mineral proportions (Fig.3 and 4, Table 1).

#### 249 **4.1.1. Western Lelukuau: sample 135A**

250 Sample 135A is a homogeneous granoblastic rock which, in addition to the main mineral  
251 assemblage, also contains rare biotite, quartz, zircon, and apatite (Figs. 3a and 4a, Table 1).  
252 Garnet is subhedral, ranging in size from 2 to 4 mm and containing rare inclusions of kyanite,  
253 zircon, or apatite. It is chemically characterized by  $X_{Mg} = 0.54\text{--}0.57$  and  $X_{Grs} = 0.21\text{--}0.29$ , both  
254 parameters decreasing towards the rims (Figs 4a, 5a, 6a, b, c). Clinopyroxene is light green  
255 subhedral and up to 1 mm in size (Fig.5c). It has a diopside composition, with up to 10 % Ca-  
256 Tschermak component, regardless the textural position, and 7–13% jadeite, uniform at the  
257 grain scale. Clinopyroxene in contact with garnet systematically shows a higher Si content  
258 (1.90–1.92 apfu), and all grains display Al enrichment in the core and Mg enrichment in the  
259 rims. Plagioclase is subhedral with a grain size ranging from 0.2 to 0.5 mm. Its anorthite  
260 component ( $X_{An} = 0.35\text{--}0.50$ ) is varied at the thin-section scale, but single grains are  
261 homogeneous (e.g.,  $X_{Anpl1} = 0.43\text{--}0.44$ ;  $X_{Anpl6} = 0.35\text{--}0.36$ ;  $X_{Anpl3} = 0.45\text{--}0.47$ ; Fig. 5d).  
262 Amphibole, 0.2 to 0.4 mm in size, is exclusively associated with clinopyroxene. It is calcic  
263 ( $Ca^B = 1.84\text{--}1.93$ ,  $Na+K = 0.77\text{--}0.92$ ,  $Ti = 0.09\text{--}0.22$  apfu), Al rich ( $Al M1 = 0.76\text{--}1.27$ ), and  
264 magnesian ( $X_{Mg} = 0.73\text{--}0.78$ ; Fig. 5b). Scapolite is disseminated across the thin section and  
265 has a sylvialitic composition, with  $X_{SO4} = 0.48\text{--}0.66$  (Fig.5e and Supplementary Table 2).  
266 When the chemical formulae of the analyzed grains are recalculated following Ellis (1978) to  
267 be compared to plagioclase, they show a significantly distinct composition of  $X_{eqAn}$  of 0.59–  
268 0.70 (Fig.5d), homogeneous at the grain scale. Rare biotite (1.5%) is observed without  
269 specific textural position. Quartz, zircon, and apatite are dispersed at the thin section scale.

#### 270 **4.1.2. Eastern Lelukuau: samples KW4A and KW4C**

271 Samples KW4C and KW4A are metagabbros collected a few meters away from each other on  
272 the same outcrop and have broadly similar chemical compositions (Supplementary Table 1).  
273 Texturally, both are granoblastic but KW4A is homogeneous and fine-grained (<0.5 mm)

274 while KW4C is medium-grained (0.5–3 mm) and has polycrystalline plagioclase domains and  
275 garnet porphyroblasts, as illustrated by the SEM–MLA maps (Fig.3b and c).

276 Sample KW4C – Subhedral plagioclase (0.15– 0.5 mm) forms polycrystalline domains (up to  
277 1 cm) that are zoned with  $X_{An} = 0.52 - 0.80$ , decreasing from the cores toward the rims  
278 (Fig.5d, Supplementary Table 2), but have a homogeneous grain size. The inner zones of the  
279 domains contain rare kyanite inclusions and are locally altered to sericite. Garnet forms  
280 subhedral grains of 0.5–2 mm, clustered into up to 4 mm composite grains (Fig.3b; Fig.6e, f,  
281 h, i). Garnet cores have abundant inclusions of kyanite needles (up to 250  $\mu\text{m}$ ) and rare quartz  
282 inclusions while the rims are inclusion-free (Fig.4b; Fig.6d to i). Garnet cores are Ca-rich with  
283  $X_{Grs} = 0.26-0.29$ ,  $X_{Prp} = 0.46-0.48$ , and  $X_{Alm} = 0.22-0.24$  while the borders (including those  
284 of the subgrains) are enriched in Fe–Mg and show Ca depletion ( $X_{Grs} = 0.19-0.21$ ,  
285  $X_{Prp} = 0.52-0.57$ ,  $X_{Alm} = 0.25-0.29$ ) with this trend being more pronounced at the outer rims  
286 of the composite grains (Figs. 5a, 6e, f, h, i). Clinopyroxene forms anhedral grains of 0.5 to 1  
287 mm, that are locally associated with quartz and plagioclase and/or amphibole in large  
288 aggregates of 1 to 2 mm. It has a diopside composition, with 5 to 8% jadeite and 2 to 10% Ca-  
289 Tschermak (Fig.4b, 5c). They all display Al enrichment in cores and Mg enrichment in rims.  
290 Amphibole forms subhedral grains with embayed borders, closely associated to clinopyroxene  
291 and, rarely, in the middle of plagioclase domains. Single grains are ca. 0.15–0.40 mm in size,  
292 but locally form 2 mm elongated aggregates. Amphibole has edenitic composition with  
293  $\text{Ca}^B = 1.88-1.93$ ,  $\text{Na}+\text{K} = 0.53-0.64$ ,  $\text{Ti} = 0.09-0.2$  apfu,  $\text{Al M1} = 0.97-1.32$  and  $X_{Mg} = 0.85-$   
294  $0.87$  (Fig.5b). The Si content varies from 6.50 to 6.89 apfu in all the analyzed grains but  
295 doesn't reflect any general trend or textural position specificity. Quartz is only found in three  
296 textural positions, either as rare inclusions in garnet, entrapped in the inner zones of garnet  
297 composite grains, or associated to clinopyroxene (Fig. 6d, g). Scapolite grains are dispersed in  
298 the thin section and commonly associated with garnet or plagioclase. They have a meionite

299 composition with  $X_{SO_4} = 0.28\text{--}0.37$  (Fig. 5e and Supplementary Table 2). When recalculated  
300 following Ellis (1978) to be compared to plagioclase (Fig., 5d), scapolite shows an  
301 intermediate composition of  $X_{eqAn}$  of  $0.65\text{--}0.69$  and are homogeneous at the scale of the grain.  
302 Kyanite is found in two textural positions: i) as needle inclusions in garnet and ii) locally in  
303 the center of high-Ca plagioclase domains.

304 Sample KW4A – Plagioclase forms euhedral grains, 0.2–0.4 mm in size, that are  
305 homogeneous throughout the thin section, with  $X_{An} = 0.35\text{--}0.24$  (Fig. 3c, 5d, 6j to l) and  
306 Supplementary Table 2). Locally, K-feldspar exsolutions are observed in the plagioclase  
307 domains (<1%). Garnet forms grains mostly 0.5 mm in size that are commonly clustered into  
308 3 mm-wide composite grains, homogeneously distributed across the thin section. Grains show  
309 complex zoning (Fig.5a, 6j to l), some subgrains being Ca-rich ( $X_{Grs} = 0.23\text{--}0.25$ ,  $X_{Prp} = 0.35\text{--}$   
310  $0.36$ ,  $X_{Alm} = 0.39\text{--}0.41$ ) while others are Fe–Mg-rich ( $X_{Grs} = 0.19\text{--}0.22$ ,  $X_{Prp} = 0.38\text{--}0.41$ ,  
311  $X_{Alm} = 0.37\text{--}0.41$ ). Clinopyroxene forms subhedral grains, 0.2–0.5 mm in size. It has diopside  
312 composition, 7 to 11% jadeite and up to 10% Ca-Tschermak component, while total Al is low  
313 ( $0.18\text{--}0.41$  apfu). Scapolite is euhedral, 0.2 to 0.5 mm in size, and is homogeneously  
314 distributed at the thin section scale. It has a sylvialitic composition ( $X_{SO_4} = 0.50\text{--}0.70$ , Fig. 5e)  
315 and commonly clusters in larger domains up to 3 mm. Rare amphibole or quartz are dispersed  
316 at the thin section scale.

#### 317 **4.1.3. Mineral assemblages and background to the phase equilibria modelling**

318 The three samples are composed of varied amounts of garnet, clinopyroxene, and plagioclase  
319 that are characteristic of high-P granulite facies conditions. Samples 135A and KW4C, that  
320 are medium grained, also show a  $X_{Alm}$  increase in the garnet rim that is consistent with  
321 diffusional re-equilibration of the rims during cooling. Because of high peak temperatures  
322 attained and/or maintained in granulite facies rocks, the prograde history can be deciphered  
323 mostly by mineral inclusions. To this end, KW4C provides a snapshot in the crystallization of

324 kyanite and quartz during an early part of the P–T path associated with plagioclase  
325 destabilization and garnet crystallization following the reaction anorthite = grossular +  
326 kyanite + quartz, at high-P conditions. Moreover, in this sample, the large, recrystallized  
327 plagioclase domains are interpreted to pseudomorph former igneous plagioclase, preserving  
328 original Ca-rich core and Na-rich rims. Rare kyanite included in garnet of sample 135A,  
329 suggests a similar reaction history.

330 According to the literature, scapolite, and specifically S-scapolite, can either be (i) an igneous  
331 phase (e.g., Boivin & Camus, 1981), (ii) result from plagioclase alteration (e.g. Touret &  
332 Nijland, 2013), or (iii) be a metamorphic mineral (e.g., by replacement of igneous plagioclase:  
333 Austheim, 2013). Given the textural evidence of pervasive granoblastic recrystallisation, the  
334 magmatic phase option can be ruled out. If the scapolite were an alteration phase of  
335 metamorphic plagioclase, then the  $X_{\text{eqAn}}$  would be spread along the same range given that  
336 scapolite grains are not observed in one specific textural position. In all samples, scapolite  
337  $X_{\text{eqAn}}$  is different from  $X_{\text{An}}$  of plagioclase, and they are consequently interpreted as part of the  
338 main metamorphic assemblage. This would require either a S-bearing mineral breakdown  
339 during prograde metamorphism, or a S-bearing fluid phase at high-pressure.

340

#### 341 **4.2. P-T estimates**

342 Samples 135A and KW4A were used to calculate P–T pseudosections. MnO, K<sub>2</sub>O and TiO<sub>2</sub>  
343 were removed from the bulk-rock composition since their amounts are low in the bulk rock  
344 (less than 0.65 wt.%; see Supplementary Table 1), and they consequently will not impact the  
345 modelled stability of the main mineral assemblage present. For both calculations,  $\text{Fe}^{3+}/\text{Fe}^{\text{tot}}$   
346 was set at 0.1 while H<sub>2</sub>O was calculated based on the proportion of amphibole in the rock.  
347 Scapolite is part of the mineral assemblage and represents ca. 5 %. As no solid-solution model  
348 was available, two approaches were considered: (i) scapolite was treated as plagioclase; and

349 (ii) scapolite was removed from the bulk-rock composition by subtracting the equivalent  
350 amount of CaO, Na<sub>2</sub>O, Al<sub>2</sub>O<sub>3</sub> and SiO<sub>2</sub>. Considering all scapolite as plagioclase results in  
351 excess Al and Si, that impacts the Al–Si-bearing-mineral stability, either over-estimating  
352 quartz or kyanite, but also over or under-estimating garnet, plagioclase, and clinopyroxene  
353 modal proportions. Subtracting a mineral from a bulk rock composition is a common practice  
354 to account for the lack of a solution model for some phases and is often used to correct for the  
355 Ca content of apatite (see LaSalle and Indares, 2014, Lotout et al., 2018, 2020). Subtracting a  
356 minor phase from the bulk is unlikely to influence rock-forming reactions, but it is an  
357 oversimplification for major phase that *de facto* modifies the thermodynamic equilibrium state  
358 of each assemblage. Both solutions have been tested, and we present results calculated from  
359 an unmodified bulk, i.e., not removing scapolite from the bulk-rock composition, as it  
360 provides the best fit.

361 Western-Lelukau – For sample 135A, the stability field of the peak assemblage garnet–  
362 diopside–plagioclase–amphibole is limited by the appearance of liquid at higher T and kyanite  
363 at higher P–T conditions (Fig. 7a). Quartz is stable at P–T conditions between 700°C/12 kbar  
364 and 900°C/14 kbar, with modal proportion < 2 %, in good agreement with the observed  
365 mineral proportion (Table 1). In the P–T pseudosection, amphibole has a pargasitic  
366 composition, with modal proportions (12 to 8 %) decreasing gradually towards the melt-in  
367 line. The plagioclase-out line at ca. 700°C/16 kbar and 850°C/19 kbar marks the limit  
368 between the high-P granulite and the eclogite facies. The calculated modal proportions of  
369 garnet and clinopyroxene (Fig. 7a, Table 1), the X<sub>Mg</sub> of garnet and the grossular isopleth (Fig.  
370 7b), together with the kyanite and melt boundary lines, restrict the stability field of the  
371 assemblage between ca. 770°/14 kbar and 870°C/16 kbar, with garnet rims crystallizing in the  
372 lower P and T part of this stability field. The calculated modal proportion of plagioclase is

373 however higher than the measured proportions, which is attributed to the exclusion of  
374 scapolite from the modelling.

375 Eastern-Lelukauu – Sample KW4C could not be successfully modelled because it is too  
376 dominated by local equilibria texture. In contrast, sample KW4A is well equilibrated at the  
377 thin section scale and the garnet–clinopyroxene–plagioclase–quartz assemblage is stable in a  
378 large P–T field from 700 to 900°C and up to 17 kbar, delimited by the kyanite-in and liquid-in  
379 lines at lower and higher temperatures, respectively (Fig.7c). Calculated modal proportions of  
380 clinopyroxene, garnet and plagioclase don't match the observed mineral proportion in thin  
381 section. This could be the result of re-equilibration during cooling.

382

### 383 **4.3. Garnet petrochronology**

384 Samples 135A and KW4C were analyzed using the Lu–Hf and Sm–Nd garnet dating method.  
385 A summary of the results is presented in Table 2 and plotted in Figure 9. Garnet fractions 1 to  
386 4 were spiked for both Lu–Hf and Sm–Nd, while garnet fractions 5 and 6 were only spiked  
387 for Lu–Hf analysis. For each sample, two representative whole rocks were also spiked for Lu–  
388 Hf and Sm–Nd, and followed partial (WRS – Whole Rock Savillex; tabletop) and complete  
389 (WRB – Whole Rock Bombed; Parr-bomb vessel) digestion procedures. One clinopyroxene  
390 fraction was also analyzed for sample 135A. Single Lu–Hf or Sm–Nd dates were calculated  
391 for each mineral fraction by pairing them to the WRB (2-pt ages). For each sample, a  
392 representative trace element (TE) profile normalized to chondrite is presented in Fig.8.

#### 393 **4.3.1. Western Lelukauu: sample 135A**

394 The Lu, Sm and Nd contents from sample 135A are mostly below 1 ppm across garnet grains,  
395 and increase from core to rim, from 0.2 to 1 ppm, 0.4 to 1.6 ppm and 0.4 to 1.1 ppm,  
396 respectively (Fig. 8a and Supplementary Table 3). Hf contents range from below the detection

397 limit to 0.3 ppm through garnet grains, at the limit of detection and with no specific pattern.  
398 Gd/Yb ratios are systematically highest at the rims, at 0.9 to 2.2, while internal zones vary  
399 from 0.2 to 0.8. The atypical Lu-depleted core and Lu-enriched rim could be the result of a  
400 Lu-rich phase (such as zircon) reacting out during garnet growth. Garnet residues from the  
401 dissolution procedure were mostly composed of rare quartz or clinopyroxene inclusions,  
402 except of fraction 4 where a single zircon grain was found (z-Rg4, later subjected to U–Pb *in*  
403 *situ* dating).

404 The six garnet aliquots represent a well averaged population, with Lu and Hf contents (0.58–  
405 0.60 ppm and 0.13–0.14 ppm respectively; Table 2) similar to those obtained by *in situ*  
406 measurements. The WRS and WRB show a significant difference in both Lu and Hf content  
407 highlighting the contribution of zircon (e.g., Scherer et al., 2000). Two-point isochrons, using  
408 the WRB fraction and garnet fractions 2, 3, 5 and 6, range from  $1022.2 \pm 6.1$  to  
409  $1018.4 \pm 6.3$  Ma, and generate a mean date of  $1020.3 \pm 3.0$  (MSWD = 0.34, Table 2).  
410 Fractions 1 and 4 show slightly younger dates of  $1009.3 \pm 6$  Ma and  $997.1 \pm 6$  Ma,  
411 respectively. With respect to fraction 4, all the two point garnet-whole rock isochron dates  
412 yielded similar results within error when paired with the clinopyroxene, the WRS, or the  
413 WRB fractions, at ca.  $1018 \pm 6.8$  Ma (MSWD = 3.6; Fig. 9a). Garnet fractions 1, 2, 3, 5 and  
414 6, the clinopyroxene fraction, and both whole rocks define an eight-point isochron date of  
415  $1019.9 \pm 6.8$  Ma (MSWD = 2.7; Fig 9a). Including fraction 4 in the calculation results in a  
416 date of  $1016 \pm 14$  Ma with higher MSWD of 8.7 reflecting excess scatter. Excluding fraction  
417 1 and 4 results in a 7-point isochron age of  $1022 \pm 3.2$  Ma with a slightly lower MSWD of  
418 0.94.

419 Sm and Nd contents from the four garnet aliquots range from 1.54 to 1.60 ppm and from 2.19  
420 to 2.74 ppm respectively (Table 2). The WRS and WRB fractions have significantly distinct  
421 Sm and Nd concentrations, but almost identical  $^{147}\text{Sm}/^{144}\text{Nd}$  and  $^{143}\text{Nd}/^{144}\text{Nd}$ . This highlights

422 that, despite a contribution from a Sm- and Nd-rich refractory phase during the dissolution  
423 procedure in bomb, the sample was well equilibrated and wasn't later disturbed by alteration  
424 or Sm- or Nd-rich fluid. Altogether, the data align on an isochron that corresponds to a date of  
425  $1005 \pm 13$  Ma (MSWD = 0.25; Fig 9b), overlapping within error with the Lu–Hf results.

#### 426 **4.3.2. Eastern Lelukuau: sample KW4C**

427 Chondrite-normalized REE patterns for sample KW4C show HREE-enriched cores and  
428 MREE-enriched rims across garnet grains (Fig. 8b), typical of preferential incorporation of  
429 HREEs during garnet early-growth (e.g., Otamendi et al., 2002). Garnet cores also show  
430 higher LREE concentrations compared to the mantle and rim zones. The Lu contents decrease  
431 from core to rim, from 0.4 to 0.1 ppm, and Hf content was systematically below 0.1 ppm to  
432 below the detection limit. Sm systematically shows two pulses of concentration increases,  
433 separated by a lower concentration, from ca. 0.4 to 1 ppm, followed by a 0.2 to 1.2 ppm zone,  
434 and 0.1 to 1 ppm (Supplementary Table 3). The positive Eu anomaly in the whole rock (1.86)  
435 is not observed consistently in the garnet, with maximum values in the garnet cores (1.1 to  
436 2.0) and lowest values in garnet rims (0.9 to 1.4). Finally, the rim shows distinct REE pattern  
437 differences from the core of garnet, and lack continuous depletion; instead, two population are  
438 observed (Fig. 8b).

439 All residues from garnet dissolution procedures included variable amount of kyanite and  
440 quartz needles, fractions 5 and 6 being 10 times richer than fractions 1, 4 and 5, while fraction  
441 2 has an intermediate amount. Lu and Hf contents for the six garnet fractions are similar, at  
442 0.21–0.22 ppm and 0.07–0.08 ppm respectively, and corresponding  $^{176}\text{Lu}/^{177}\text{Hf}$  and  
443  $^{176}\text{Hf}/^{177}\text{Hf}$  show little variation (Table 2). WRS and WRB fractions yield equivalent Lu and  
444 Hf contents of 0.06 ppm and 0.32–0.34 ppm, showing that no Hf or Lu-rich phase  
445 contributed. However, isotopic ratios are not identical, possibly resulting from an incomplete  
446 spike-sample equilibration in the savillex tabletop fraction (WRS). The garnet Lu–Hf 2-point

447 isochron dates for fractions 2, 5 and 6 are  $1023.9 \pm 7.8$  Ma,  $1029.1 \pm 7.9$  Ma and  
448  $1036.8 \pm 7.9$  Ma, resulting in an average date of  $1029.9 \pm 4.6$  Ma (MSWD = 2.7). Garnet  
449 fractions 1, 3 and 4 resulted in 2-point isochron dates of  $1014.6 \pm 7.8$  Ma,  $1011.9 \pm 6.6$  Ma  
450 and  $1013.0 \pm 7.8$  Ma, respectively, and corresponding average date of  $1013.0 \pm 4.2$  Ma  
451 (MSWD = 0.87). Including all 6 of these dates result in a mean date of  $1021 \pm 11$  Ma, with an  
452 expectedly high MSWD of 7. The 2-point date of garnet fraction 2 is intermediate at  
453  $1023.9 \pm 7.9$  Ma, overlapping within error with all garnet fractions, corresponding to an  
454 averaged population of two garnet endmembers. Altogether, the 9 fractions define an isochron  
455 age of  $1018 \pm 18$  Ma (MSWD = 8.1), reflecting scatter along the isochron due to the  
456 variability observed in the garnet isotopic compositions. If we consider only the fractions with  
457 similar 2-point dates to calculate two separate isochrons, garnet fractions 1, 3, and 4  
458 correspond to an isochron date of  $1013.2 \pm 5.6$  Ma (MSWD = 0.14) and garnet fractions 5 and  
459 6 correspond to an isochron date of  $1033 \pm 6.3$  Ma (MSWD = 2.4; Fig. 9c).

460 Sm and Nd contents of the four garnet aliquots are low, 0.70–0.75 ppm and 0.77–0.86 ppm  
461 respectively (Table 2). WRS and WRB aliquots yielded almost identical Sm and Nd  
462 concentrations of 1.08 and 1.09 ppm and 4.88 and 4.93 ppm, respectively, and corresponding  
463 isotopic ratios are also identical within error. This indicates there was no contribution from a  
464 Sm or Nd rich phase during the dissolution procedure in bomb, and Sm-Nd homogeneity  
465 within the sample. Moreover, this is also independent evidence for reproducibility of the  
466 results, emphasizing the absence of contamination in the overall dissolution and column  
467 procedure. All fractions correspond to an isochron date of  $1003.0 \pm 8.3$  Ma (MSWD = 0.07;  
468 Fig. 9d), with a good alignment of the 8 points; the limited spread in the data is responsible  
469 for the elevated error and very low MSWD.

470

#### 471 **4.4. Zircon petrochronology**

472 Zircon was only found in sample 135A from western-Lelukau. Six zircon grains were  
473 analyzed directly in thick section and 14 zircon grains were handpicked from whole rock  
474 mineral separate. Colorless zircon crystals are 60 to 200  $\mu\text{m}$  in size, with variable shapes from  
475 subhedral and elongated to anhedral grains. They all have a CL-bright rim of 1 to 60  $\mu\text{m}$ , and  
476 1 to 2 inner darker CL zones, some with a well-defined core. Some zircon grains show  
477 complex textures, including fluid pathways across CL-zones (Fig.10, 135A-2-Z2; Z4), and  
478 cracks in the external rim (Fig.10, 135A-1z3, 135A-5-z2b). Few cores present an oscillatory  
479 zonation (Fig.10, Z1, Z6, Z8 and Z10). Forty-seven U–Pb analyses and 34 REE analyses were  
480 acquired on distinct CL zones from these 20 zircon grains. Amongst the U–Pb data, 3  
481 analyses were excluded due to high common lead contents ( $P_{bc} > 3\%$ ), the remaining 44  
482 analyses showing a  $P_{bc}$  content  $< 0.7\%$  in most cases, with one outlier at 2.2 %. Uranium  
483 contents are variable, spreading from 12 to 2623 ppm and Th/U ratios range from 0.02 to  
484 1.83, this ratio showing the maximum spread for cores (ca. 0.4 to 1.7, Fig.11c). Analyzed  
485 zircon zones are discordant to sub-concordant (92 to 99 % concordance, Fig 11a), and the  
486  $^{207}\text{Pb}/^{206}\text{Pb}$  ages spread from ca 1.00 to 1.65 Ga (Fig. 11b, d). In cores and rims, the Lu  
487 concentrations vary from 0.5 to 96 ppm independently from the corresponding Eu\* anomaly  
488 (Fig.11f), which spreads from 0.7 to 1.1. Chondrite-normalized REE patterns are similar with  
489 enriched HREE and no to small Eu\*, in both cores and rims ( $\text{Eu} = 0.78\text{-}1.08$ , Fig.11e). Three  
490 spectra obtained in ca. 1.2 Ga rims show flat HREE pattern (Fig. 11e and Fig 10).

491 Zircon cores are composed of two  $^{207}\text{Pb}/^{206}\text{Pb}$  population, at ca. 1.6 and 1.4 Ga, without any  
492 specific distinction in U, Th, or REE contents (Fig. 11c, d, e, f). Average  $^{207}\text{Pb}/^{206}\text{Pb}$  dates  
493 calculated on ca. 1.6 Ga cores yields a mean date of  $1630 \pm 12$  Ma ( $N = 13$ ,  $\text{MSWD} = 53$ ) and  
494 an upper intercept date of  $1653 \pm 33$  Ma ( $N = 13$ ,  $\text{MSWD} = 32$ ). Two cores and 4 rims  
495 (Fig.10, core: z2 and z12, rims z3, z8, z9, z2b) yield an average  $^{207}\text{Pb}/^{206}\text{Pb}$  date of  
496  $1415 \pm 9$  Ma ( $N=6$ ;  $\text{MSWD} = 3.3$ ) and an upper intercept of  $1429 \pm 9$  Ma ( $\text{MSWD} = 0.69$ ).

497 Six rims provided an average  $^{207}\text{Pb}/^{206}\text{Pb}$  date of  $1184 \pm 9.1$  Ma (MSWD = 0.72, N = 6) and  
498 corresponding upper intercept of  $1239 \pm 76$  Ma (MSWD = 0.13). However, the corresponding  
499 trace element patterns are variable, with either enriched HREE or flat HREE patterns (Fig.  
500 11e), and their Th/U ratio is also varied (Th/U = 0.11 to 0.47, U = 17-264 ppm). No  
501 consistency could be observed between the remaining zircon analysis.

502

## 503 **5. General discussion and geodynamic implications**

### 504 **5.1. P-T conditions and equilibrium in HP mafic granulite**

505 The studied samples KW4A, KW4C, and 135A are textbook high-P granulites. However,  
506 assessing their peak P–T conditions is limited by: (a) the preservation of microdomains with  
507 restricted scale of equilibration likely due to a low amount of H<sub>2</sub>O, which is a catalyst in  
508 mineral reactions; and (b) the scarcity of quartz, which promotes mineral reactions in mafic  
509 rocks, leading to wide P–T stability fields of the peak assemblage.

510 Among the two modelled rocks, sample 135A, from the western Lelukau, provided the  
511 tightest P–T constrains. Modal proportions of phases calculated using P–T pseudosections of  
512 the bulk rock composition including scapolite (which is inferred to be part of the main  
513 assemblage) are consistent with the mineral proportions observed in the sample. Only slight  
514 discrepancies in plagioclase (25–30 % instead 22 %), and quartz (up to 1.5 % instead of  
515 < 0.5 %) are noted while the calculated clinopyroxene and garnet modal proportions are  
516 within <10% compared to the proportions derived from SEM–MLA. Isopleths of  $X_{\text{Mg}}$  and  
517  $X_{\text{Grs}}$  in garnet are compatible with EMPA measurements and support the calculated P–T  
518 estimates in the range between 770°/14 kbar and 870°C/16 kbar. These P–T estimates are in  
519 line with available data on kyanite bearing anatectic rocks from the southern LT (e.g.,  
520 14.5 kbar and 870–900°C, Lasalle and Indares, 2014), and with petrographic observations that

521 place the assemblages of both aluminous and mafic rocks in the high-P granulite field. In the  
522 calculated pseudosections, the liquid-in line at  $P < 18$  kbar, is between 900 and 950°C, close to  
523 the minimum peak T of 875°C for aluminous anatectic rocks from southern LT (Lasalle and  
524 Indares, 2014). The lack of partial melting in the samples is attributed to the scarcity of H<sub>2</sub>O-  
525 bearing phases. The slight discrepancy between the calculated temperature in metamafic and  
526 aluminous migmatite is within the range of uncertainty of P–T modelling.

527 The sample from eastern Lelukuau (KW4C), that preserves inherited zonation of the original  
528 igneous plagioclase, is dominated by local equilibria that makes it unsuitable for modelling,  
529 but it provides clues on the prograde history. Quartz and kyanite inclusions in garnet cores,  
530 together with garnet major element zoning, are consistent with a prograde portion of the P–T  
531 path, through the kyanite stability field. In addition, the sharp boundaries of the inclusion-  
532 bearing cores, in conjunction with the REE zoning, are consistent with two-stage garnet  
533 growth (Fig. 6e, f, h, i; Fig 8b).

534 Textural equilibrium in the absence of chemical equilibrium suggests short-term residency  
535 under high-grade conditions. Preservation of garnet prograde zoning, absence of retrograde  
536 textures, preservation of S-scapolite and preservation of igneous zoning in recrystallized  
537 plagioclase domains is consistent with fast cooling following the thermal peak. In addition,  
538 the absence of retrograde textures testifies to a fluid-poor environment during cooling and  
539 decompression.

540

## 541 **5.2. From ages to stages**

### 542 **5.2.1. Garnet petrochronology**

543 Western Lelukuau: sample 135A

544 In this sample, WR, clinopyroxene, and garnet fractions (excluding g4 for Lu–Hf) align and  
545 yield a low MSWD isochron age for the two isotopic systems, which indicates closed system  
546 evolution following equilibration. Together with petrographic and P–T evidence for high- P-  
547 granulite-facies conditions, and with the Lu–Hf and Sm–Nd ages overlapping within error at  
548  $1019.9 \pm 6.8$  Ma (MSWD = 0.94) and  $1005 \pm 13$ Ma (MSWD = 0.25), respectively, this  
549 provides an age for the peak metamorphism of the Western Lelukuau Terrane. The Lu–Hf  
550 ages are systematically skewed toward garnet early growth (e.g., see Anczkiewicz et al, 2007;  
551 Lotout et al., 2018, Tual et al., 2022) and the Lu–Hf isotopic system has a higher closure  
552 temperature than Sm–Nd (see Smit et al., 2013), which is particularly important in high-T  
553 terranes. Given the ca.  $\pm 7$  Ma uncertainty on the isochron and the  $\sim 800$ - $900^\circ\text{C}$  peak  
554 metamorphic temperatures, and despite that Lu–Hf and Sm–Nd ages slightly overlap, we  
555 interpret the garnet Lu–Hf age to approximate garnet growth and crystallization at ca.  
556 1020 Ma, and the garnet Sm–Nd age to approximate subsequent, fast cooling at ca. 1005 Ma  
557 at lower P. The preserved zoning pattern in garnet with increasing Lu towards the rims, is  
558 atypical, compared to the classic Lu-rich core to Lu-poor-rim resulting from Rayleigh  
559 fractionation. Breakdown of a HREE-rich phase during garnet growth is most likely  
560 responsible for this pattern. Given the low Lu concentration in garnet, and the fact that zircon  
561 cores are rich in Lu (up to 1000 times more), zircon breakdown during garnet growth could be  
562 sufficient to release enough Lu inducing such garnet zoning.

#### 563 Eastern Lelukuau : sample KW4C

564 The Eastern Lelukuau sample preserves petrographic evidence of two-stage garnet growth,  
565 that is corroborated by trace element zoning. The variable amount of kyanite needles and  
566 quartz crystals in the residues from the different garnet fractions, together with the two mean  
567 Lu-Hf age clusters, allow the interpretation of the older age of  $1033 \pm 6.3$  Ma as  
568 approximating first garnet growth, within the kyanite stability field. The younger Lu–Hf date

569 of  $1013 \pm 5.6$  Ma is interpreted to estimate the age of the second garnet growth. The latter  
570 also overlaps within error with the Sm–Nd date of  $1003 \pm 8.3$  Ma. Given the petrographic  
571 record, this date is interpreted to reflect cooling of the terrane at lower pressure.

572

### 573 **5.3. Zircon ages**

574 Zircon was only retrieved in sample 135A, and shows a complex history. The U–Pb dataset is  
575 consistent with continuous or multiple lead loss event, and, potentially, several ages of zircon  
576 growth. The oldest age of 1.6 Ga from 16 zircon cores is in good agreement with the ca.  
577 1631 Ma age of a gabbro-troctolite from the AMCG suite in the same area (Indares et al.,  
578 1998). Additional zircon growth episodes at ca. 1.4 Ga and 1.2 Ga are deduced from the  
579 textures and the  $^{207}\text{Pb}/^{206}\text{Pb}$  ages. The similarities between the REE patterns in the different  
580 CL zones with different  $^{207}\text{Pb}/^{206}\text{Pb}$  dates, and the large variability in the elemental record of  
581 CL zones recording similar dates, could be attributed to partial dissolution-reprecipitation of  
582 igneous zircon below the solidus. This would reset the age but preserve the initial REE  
583 signature and new growth, both variably affected by lead loss during metamorphism.  
584 Moreover, the Eu\* and Lu content are not linked to a specific CL texture.

585 Only a few zircon rims are of Grenvillian age, and they are mostly discordant. The Eu\*  
586 anomaly is consistently low to absent, from 0.8 to 1.2. This could suggest absence of  
587 plagioclase (e.g., Rubatto 2002, 2017; Whitehouse and Platt, 2003) and/or growth of garnet  
588 that fractionate  $\text{Fe}^{2+}$  over  $\text{Fe}^{3+}$ , changing the overall oxidation state and converting  $\text{Eu}^{2+}$  to  
589  $\text{Eu}^{3+}$  (e.g., Tang et al., 2018). In both cases, it would imply crystallization of zircon under  
590 high-pressure, at 1.6, 1.4 and 1.2 Ga. However, zircon show classic HREE-enrichment,  
591 typical of crystallization in a garnet-absent assemblage, which contradicts this interpretation.  
592 Another way to interpret this dataset would either be for zircon to 1) crystallize before or  
593 during early plagioclase crystallization, 2) crystallize in an oxidized magma, or 3) crystallize

594 from kinetic disequilibrium, as has been invoked for Eu\* anomalies in clinopyroxene (see  
595 Tilhac et al., 2023). Option 1 can easily be ruled out, as late-stage crystallization of zircon  
596 from a local high differentiated pocket of magma are needed to crystallize zircon in Zr under-  
597 saturated mafic magmas. Given the homogeneous REE patterns, kinetic disequilibrium seems  
598 unlikely, and an oxidized magma appears to be a preferable option.

599 Ages at 1.4 and 1.2 Ga are well known in Tshenukutish Terrane and in the Mid-P belt to the  
600 south. 1.4 Ga corresponds to a major crust forming event (Pinwarian), whereas 1.2 Ga is the  
601 time of localized extensional episodes (see review in Indares, 2020). However, it seems  
602 unlikely that these events would have promoted metamorphic zircon growth in the dry MIZ  
603 protoliths. Considering that sample 135A has no record of inherited gabbroic textures, an  
604 alternate explanation for the variability in the zircon dataset would be that the protolith of this  
605 sample is a mafic supracrustal rock with a sedimentary component rather than a plutonic rock,  
606 and that the zircons are detrital. This is also supported by the large range of Th/U ratio at  
607 distinct dates, that could suggest variable zircon sources.

608 Finally, regardless of the protolith nature of the sample and only looking at recorded dates,  
609 zircon did not successfully recrystallize during the high P–T event. The absence of partial  
610 melting and the dryness inherent to mafic high-P granulite is a plausible explanation for  
611 zircon’s rare reactions despite the high P–T metamorphism that occurred at 1020 Ma.

612

#### 613 **5.4. Overall metamorphic patterns in the MIZ and tectonic implications**

614 The new garnet ages reported in this study provide important constraints on the  
615 metamorphism of the MIZ since they are derived from mafic rocks from the LT, that make up  
616 its largest lithotectonic component. The Lu– Hf ages, at ca. 1033 Ma, with a second garnet  
617 growth at ca 1013 Ma in the eastern LT sample and at ca. 1020 Ma in the western LT sample,

618 suggest that the high-P granulite assemblage formed during the late Ottawaan straddling the  
619 Ottawaan-Rigolet hiatus. They also suggest that there may be diachronism in garnet growth  
620 from East to West. In addition, the Sm-Nd isotope data are consistent with rapid cooling at ca.  
621 1005 – 1003 Ma.

622 These ages are younger than the monazite dates from an aluminous anatectic rock in southern  
623 LT (ca. 1060 – 1044 Ma, Dunning and Indares 2010; Lassalle et al., 2014), however, the  
624 previously published ages are difficult to interpret because of strong inheritance.

625 Nevertheless, taken together, these data suggest a potential younging of the age of  
626 metamorphism from the southern boundary of LT to the north, towards the Parautochthonous  
627 Belt.

628 Anatectic aluminous rocks from the Tshenukutish Terrane, at the SSE margin of the MIZ,  
629 were subjected to similar high-P metamorphic conditions (Indares et al., 2008; Lasalle and  
630 Indares, 2014; Kendrick and Indares, 2018) and show well constrained monazite ages from  
631 ca. 1040 to 1017 Ma, interpreted to approximate the age of high-P metamorphism. These ages  
632 are younging to the east, towards the boundary of the Tshenukutish Terrane against the Hart  
633 Jaune terrane (Fig. 1c), and were interpreted to represent progressively later incorporation of  
634 tectonic slivers in the slice stack (Indares 2020). In contrast, ages of mid-P granulite facies  
635 metamorphism, in the structurally overlying mid-P belt in the Manicouagan area, range  
636 between ca. 1080 and 1040 Ma, i.e. they are early to mid-Ottawan (Dunning and Indares,  
637 2010; Lassalle et al., 2014).

638 The high-P belt of the Grenville Province has been traditionally attributed to the extrusion of  
639 lower crust from beneath an orogenic plateau that developed during the early stages of the  
640 Ottawaan phase, prior to ca. 1050 Ma (e.g., Rivers, 2008, and reference therein). In this  
641 scenario, the MIZ would show similar or older metamorphic ages than the overlying mid-P  
642 belt. However, the diachronism observed in the metamorphic age pattern of the hinterland in

643 the central Grenville contradicts this interpretation, as younger, late Ottawaan transitional to  
644 Rigolet ages are recorded in the MIZ relative to the early to mid-Ottawan ages in the  
645 structurally overlying Mid-P belt. This highlights a general younging of the metamorphic ages  
646 towards the NW that is best explained by local crustal thickening in the margin of the  
647 orogenic front at the time the orogen was progressing (e.g., see Fig. 16b and c of Indares,  
648 2020). This local thickening would have been facilitated by the presence of the rigid Archean  
649 lithosphere of the Parautochthonous belt, as proposed by Indares (2020). Although the  
650 presence of a thick orogenic plateau in the central Grenville cannot be excluded, the new data  
651 show that the MIZ does not provide tangible evidence, and are in line with recent proposals  
652 for overall thin orogenic crust in the Mesoproterozoic (e.g., Spencer et al., 2021).

653 These new metamorphic ages still predate the incorporation of the Parautochthonous Gagnon  
654 terrane in the Grenville orogen during the Rigolet phase, as suggested by the ~1000–980 Ma  
655 zircon and monazite metamorphic ages from the footwall of the MIZ (Jordan et al. 2006;  
656 Jannin et al. 2018a, b). However, these ages indicate a continuum in the tectonic activity of  
657 the orogen, and discount the tectonic hiatus hypothesis traditionally inferred between the  
658 Ottawaan and Rigolet orogenic phases.

### 659 **5.5. High-P domains in the Grenville Province**

660 The characteristics of the MIZ are markedly distinct from the other two high-P segments  
661 documented in the Grenville Province (Fig.1b). In the western high-P segment, eclogite pods  
662 in orthogneisses (Davidson, 1990) have metamorphic ages as old as 1090 Ma, broadly  
663 coincident with early stages of the continental collision (Hynes and Rivers, 2010), followed  
664 by a 1080 Ma granulite-facies overprint (zircon; Marsh & Culshaw, 2014). Both the western  
665 high-P segment and MIZ belong to the Allochthonous belt and are located structurally above  
666 the Parautochthonous belt. They have been referred in the literature as the ‘high-P belt’,  
667 however, it now appears that the ages in the western segment are much older than in the MIZ.

668 They consequently correspond to different orogenic episodes and, because of this, the term  
669 “high-P belt” is not appropriate. Finally, east of the MIZ, the high-P Molson Lake terrane is  
670 part of the Parautochthonous belt, structurally below the Orogenic Lid in that area (St Joseph  
671 terrane, Connelly et al., 1995), with preliminary metamorphic ages at 1.00 Ga (see Rivers et  
672 al. 2012).

673 Collectively, the three high-P segments provide evidence of significant crustal thickening in a  
674 Mesoproterozoic orogenic setting. Although the tectonic significance of the other two  
675 segments is poorly understood, they are all exposed at the frontal parts of the orogen, and  
676 formed diachronously, defining a pattern of younging towards the Eastern part of the  
677 Grenville Province, while also getting closer to the Grenville Front.

678

## 679 **6. Conclusions**

680 High-P domains exposed in the Grenville Province provide unequivocal evidence of crustal  
681 thickening in a Mesoproterozoic orogenic setting; their characteristics, however, are far from  
682 uniform. The metamorphic patterns and tectonic significance of the Manicouagan Imbricate  
683 Zone (MIZ) explored in this study provide new insights on high-P processes in the  
684 Mesoproterozoic. The key outcomes are summarized below:

- 685 1. Mafic rocks from the Manicouagan Imbricate Zone underwent high-P granulite  
686 metamorphism of 14–16kbar and 800–900°C.
- 687 2. This study in the MIZ provides the first garnet Lu–Hf and Sm–Nd dating of high-P  
688 granulite facies of the Grenville Province. Peak of metamorphism is dated ca. 1030  
689 to 1020 Ma and followed by subsequent fast cooling, with an apparent younging of  
690 the ages towards the Grenville Front.

- 691 3. Zircon, in dry high-P mafic granulites appears to not successfully recrystallize due  
692 to lack of partial melt and hydrous phases.
- 693 4. The high-P granulite rocks in the Manicouagan Imbricate Zone are not related to  
694 the extrusion of metamorphosed lower crust during collision and building of a  
695 high-plateau during the early stage of the Ottawa phase as previously thought.  
696 Instead, it is related to local crustal thickening as the orogen propagates towards  
697 the Grenville front. Therefore, the existence of a thick orogenic plateau in the  
698 Grenville is questioned.
- 699 5. The results from this study support a tectonic continuum in between the Ottawa  
700 and Rigolet phases, and highlight the long-lived active tectonic character of the  
701 Grenville Orogeny.
- 702 6. Finally, this study highlights the diachronicity of the high-P domains of the  
703 Grenville Province, and calls for a better understanding of the overall pattern of  
704 crustal thickening at the broad regional scale of the Province.

705 Debate on the Mesoproterozoic geodynamic styles continues and spans from single lid to  
706 active tectonics. The multiplicity of tectonic scenarios for the Grenville Orogeny, and for  
707 Mesoproterozoic orogenies in general, highlights that the scarcity of P-T-t data is a barrier to  
708 comprehensive large-scale reconstructions and geodynamic interpretations.

709

710 **ACKNOWLEDGEMENTS**

711 This study is part of “CHRONOTEC – Condition and Duration of High-T event in LHO  
712 assessed through petrochronology: insights from the Grenville Tectonic”, a project funded by  
713 the European Union’s Horizon 2020 research and innovation program under the Marie  
714 Skłodowska-Curie grant agreement n°896746 to CL. CL thanks Dr. W. Aylward (MUN) for  
715 calibration at the EPMA & set up at the SEM, Dr. M. Wälle (MUN) for calibration at the LA-  
716 ICPMS, D. Goudie (MUN) for running the SEM-MLA scans, P. Baker (WSU) for assistance  
717 during isotope geochemistry, C. Knaack (WSU) for assistance during the course of the  
718 Neptune analysis, N. Bouden (CRPG) for assistance during the SIMS analysis. CL thanks S.  
719 Strowbridge for reading an early version of this manuscript. CL thanks the administrative  
720 staff at the CRPG, especially Mmes Aurélie Didot & Isabelle Geoffroy, without whom this  
721 project involving missions between 3 research labs in 3 different countries during covid time  
722 would have been even more delayed. We thank Drs Pease and Kemp for efficient editorial  
723 handling, and Dr Chacko and an anonymous reviewer for their comments and suggestions.  
724

725 **CAPTIONS**

726 Figure 1 - A. Schematic map of the Grenville Orogen in North America, B. Schematic map  
727 highlighting the tectono-metamorphic divisions of the Grenville Province, modified after  
728 Rivers et al. (2008) and Indares (2020). ABT – Allochthon Boundary Thrust. C. Schematic  
729 map highlighting the tectono-metamorphic divisions of the Manicouagan Imbricate Zone  
730 (MIZ, Central Grenville Province), modified after Indares (2020), sample location indicated.  
731 Light pink in the LT shows locations of the anatectic aluminous outcrops.

732 Figure 2 - Available ages compiled from Cox et al. (1998), Indares et al. (1998), Indares and  
733 Dunning (2001, 2004), Dunning and Indares (2010), Lasalle et al. (2014), modified from  
734 Indares and Dunning (2017). Error bars less than 5 my are not shown.

735 Figure 3 - False color mineral maps generated by Scanning Electron Microscopy and Mineral  
736 Liberation Analysis of polished thin sections, and corresponding mineral abundances. A.  
737 sample 135a, western Lelukuau terrane. B. sample KW4C, eastern Lelukuau terrane.  
738 Plagioclase: light grey (low Ca) to dark grey (high Ca). Garnet: pink (low Ca) to burgundy  
739 (high Ca). C. sample KW4A, eastern Lelukuau terrane. Corresponding proportions are shown  
740 in Table 1.

741 Figure 4 – Photomicrographs of samples A. 135a, B. KW4C, C. KW4A

742 Figure 5- Compositional profiles (A) and diagrams (B to E) for the minerals from samples  
743 135A (pink), KW4C (green) and KW4A (orange). A. Garnet. B. Amphibole ( $CaB \geq 1.5$  and  
744  $(Na+K)^A \geq 0.5$ ) following the Leake et al. (1997) classification. C. Clinopyroxene. D.  
745 Plagioclase. The lighter colored symbols represent the scapolite composition recalculated as  
746 plagioclase, following Ellis (1978). E. Scapolite.

747 Figure 6 - SEM pictures (A, D, G and J) and X-ray maps for Ca (B, E, H, K), Fe (C, F, L) and  
748 Mg (I) of garnet grains for samples 135A, KW4C, KW4A. Abbreviations are listed in the  
749 methodology section.

750 Figure 7 : P–T pseudosection calculated in the CNFMASHO system for samples 135A (A, B)  
751 and KW4A (C).

752 Figure 8 - Rare Earth Element patterns normalized to chondrite (after Sun and Mcdonough  
753 1989) acquired in garnet (yellow, magenta and blue) and for the bulk rock (black). Limit of  
754 detection in grey for the corresponding set of analysis.

755 Figure 9– (A, C) Lu–Hf and (B, D) Sm–Nd isochron diagrams for samples 135A and KW4C.  
756 WRB, whole rock bomb dissolution; WRS whole rock tabletop dissolution; g garnet; 1–6,  
757 garnet fractions; cpx, clinopyroxene. Inserts show the mean age of garnet-WRB 2-point  
758 isochrons. Zooms on the isochrons (B and D) show the reproducibility of the whole-rocks  
759 Sm-Nd analysis and (C) the scatter amongst the Lu–Hf garnet fractions and the whole rocks.  
760 “Zrn” in (A) indicate the sample in which a single grain of zircon was recovered after partial  
761 dissolution.

762 Figure 10 - Cathodoluminescence images of the analyzed zircon crystals from sample 135a  
763 (western Lelukuau), in thick section and epoxy mounts. Color-coded circles show the location  
764 of the U–Pb and REE analyses, carried out on top of each other at the SIMS.  $^{207}\text{Pb}/^{206}\text{Pb}$  dates  
765 are quoted with  $2\sigma$  uncertainty in Ma, with concordance > 90%. Th/U ratio and common lead  
766 (*italic*) are shown.

767 Figure 11 – Zircon U–Pb, Th/U, and Rare Earth Element data for the Western-Lelukuau  
768 sample (135A). A. Concordia diagram with theoretical recent lead loss and 1.0 Ga-1.6 Ga  
769 discordia line. B. Kernel density plot of  $^{207}\text{Pb}/^{206}\text{Pb}$  ages. C.  $^{207}\text{Pb}/^{206}\text{Pb}$  dates as a function of  
770 Th/U. D  $^{207}\text{Pb}/^{206}\text{Pb}$  dates, selected data used for average date calculation are highlighted. E.

771 Rare Earth Element patterns normalized to chondrite (after Sun and McDonough 1989), with  
772 color code for cores, rims and rims with an atypical pattern. F. Lu concentration as a function  
773 of the Eu\*.

774

775 Table 1 – Summary of the mineral proportion obtained by SEM–MLA on thin section of the  
776 samples 135A, KW4C and KW4A, and corresponding to Fig.3. Kyanite, rutile, zircon and  
777 apatite are below 0.5 % in all samples.

778

779 Table 2 – Summary of Lu-Hf and Sm-Nd isotopic data. Dates are produced using isoplot  
780 (Ludwig, 2003) and are reported at 95% confidence level.

781 <sup>a</sup> g – garnet fraction, cpx – clinopyroxene fraction, wrs – whole-rock savillex tabletop  
782 dissolution, wrb – whole-rock bomb dissolution.

783 <sup>b</sup> Lu, Hf, Sm, Nd concentration (ppm) obtained via isotope dilution (ca. 0.5% se).

784 <sup>c</sup> Uncertainty on the <sup>147</sup>Sm/<sup>144</sup>Nd and <sup>176</sup>Lu/<sup>177</sup>Hf ratios is estimated to be 0.5%.

785 <sup>d</sup> Within-run 2σ standard error (6<sup>th</sup> decimal), combined in quadrature with external  
786 reproducibility of spiked whole-rock samples for age regression.

787 <sup>e</sup> <sup>176</sup>Lu decay constant used for age calculation is  $1.867 \times 10^{-11} \text{ a}^{-1}$  (Söderlund et al., 2004).

788 <sup>147</sup>Sm decay constant used for age calculation is  $6.54 \times 10^{-12} \text{ a}^{-1}$  (Lugmair & Marti, 1978). 2-

789 point dates are the date obtained from a two-point isochron pairing of a single garnet fraction

790 with wrb

791 Supplementary 1 – Whole rock major (in mol.% oxide) and REE (in ppm) composition.

792 Supplementary 2 – Representative microprobe analyses of minerals.

793 Supplementary 3 – Summary of the U-Pb SIMS and REE analysis for zircon (sheet1 and 2,  
794 respectively), and REE analysis in garnet (sheet 3).

795 Appendix – Details on operating conditions, standards, chemical procedures, and solid  
796 solution models used or carried out.

797

798 **REFERENCES**

- 799 Anczkiewicz, R., Viola, G., Müntener, O., Thirlwall, M. F., Villa, I. M., & Quong, N. Q.  
800 (2007). Structure and shearing conditions in the Day Nui Con Voi massif: Implications for  
801 the evolution of the Red River shear zone in northern Vietnam. *Tectonics*, 26(2).
- 802 Austrheim, H. (2013). Fluid and deformation induced metamorphic processes around Moho  
803 beneath continent collision zones: Examples from the exposed root zone of the Caledonian  
804 mountain belt, W-Norway. *Tectonophysics*, 609, 620-635.
- 805 Baldwin, J. A., & Brown, M. (2008). Age and duration of ultrahigh-temperature  
806 metamorphism in the Anápolis–Itaçu Complex, Southern Brasília Belt, central Brazil–  
807 constraints from U–Pb geochronology, mineral rare earth element chemistry and trace-  
808 element thermometry. *Journal of Metamorphic Geology*, 26(2), 213-233.
- 809 Boivin, P., & Camus, G. (1981). Igneous scapolite-bearing associations in the Chaîne des  
810 Puys, Massif Central (France) and Atakor (Hoggar, Algeria). *Contributions to Mineralogy  
811 and Petrology*, 77(4), 365-375.
- 812 Brudner, A., Jiang, H., Chu, X., & Tang, M. (2022). Crustal thickness of the Grenville  
813 orogen: A Mesoproterozoic Tibet?. *Geology*, 50(4), 402-406.
- 814 Carignan, J., Hild, P., Mevelle, G., Morel, J., & Yeghicheyan, D. (2001). Routine analyses of  
815 trace elements in geological samples using flow injection and low pressure on-line liquid  
816 chromatography coupled to ICP-MS: A study of geochemical reference materials BR, DR-  
817 N, UB-N, AN-G and GH. *Geostandards Newsletter*, 25(2-3), 187-198.
- 818 de Capitani, C., & Petrakakis, K. (2010). The computation of equilibrium assemblage  
819 diagrams with Theriak/Domino software. *American mineralogist*, 95(7), 1006-1016.
- 820 Cawood, P. A., & Hawkesworth, C. J. (2014). Earth's middle age. *Geology*, 42(6), 503-506.

821 Cheng, H., King, R. L., Nakamura, E., Vervoort, J. D., & Zhou, Z. (2008). Coupled Lu–Hf  
822 and Sm–Nd geochronology constrains garnet growth in ultra-high-pressure eclogites from  
823 the Dabie orogen. *Journal of metamorphic Geology*, 26(7), 741-758.

824 Clowes, R., Cook, F., Hajnal, Z., Hall, J., Lewry, J., Lucas, S., & Wardle, R. (1999). Canada's  
825 LITHOPROBE Project (Collaborative, multidisciplinary geoscience research leads to new  
826 understanding of continental evolution). *Episodes Journal of International Geoscience*,  
827 22(1), 3-20.

828 Connelly, J. N., Rivers, T., & James, D. T. (1995). Thermotectonic evolution of the Grenville  
829 Province of western Labrador. *Tectonics*, 14(1), 202-217.

830 Cox, R. A., Dunning, G. R., & Indares, A. (1998). Petrology and U–Pb geochronology of  
831 mafic, high-pressure, metamorphic coronites from the Tshenukutish domain, eastern  
832 Grenville Province. *Precambrian Research*, 90(1-2), 59-83.

833 Cox, R., & Indares, A. (1999). High-pressure and high-temperature metamorphism of the  
834 mafic and ultramafic Lac Espadon Suite, Manicouagan imbricate zone, eastern Grenville  
835 Province, Quebec. *The Canadian Mineralogist*, 37(2), 335-357.

836 Davidson, A. (1990). Evidence for eclogite metamorphism in the southwestern Grenville  
837 Province. In *Current Research*, Part 1C. Geological Survey of Canada, Paper 90–1C, 113-  
838 118.

839 Deloule, E., Alexandrov, P., Cheilletz, A., Laumonier, B., & Barbey, P. (2002). In-situ U–Pb  
840 zircon ages for Early Ordovician magmatism in the eastern Pyrenees, France: the Canigou  
841 orthogneisses. *International Journal of Earth Sciences*, 91(3), 398-405.

842 Du, K. Y., Cheng, H., & Vervoort, J. D. (2021). Integrated garnet and zircon petrochronology  
843 reveals the timing and duration of orogenic events in the North China Craton. *Lithos*, 382,  
844 105939.

845 Dunning, G., Indares, A., 2010. New insights on the 1.7–1.0 Ga crustal evolution of the  
846 central Grenville Province from the Manicouagan–Baie Comeau transect. *Precambrian*  
847 *Res.* 180, 204–226.

848 Ellis, D. E. (1978). Stability and phase equilibria of chloride and carbonate bearing scapolites  
849 at 750 C and 4000 bar. *Geochimica et Cosmochimica Acta*, 42(8), 1271-1281.

850 Gasser, D., Bruand, E., Rubatto, D., & Stüwe, K. (2012). The behaviour of monazite from  
851 greenschist facies phyllites to anatectic gneisses: an example from the Chugach  
852 Metamorphic Complex, southern Alaska. *Lithos*, 134, 108-122.

853 Gervais, F., Beaudry, A., Kavanagh-Lepage, C., Moukhsil, A., Larson, K. P., & Guilmette, C.  
854 (2023). Far from boring: A new Grenvillian perspective on Mesoproterozoic tectonics.  
855 *Earth and Planetary Science Letters*, 610, 118129.

856 Green, E. C. R., White, R. W., Diener, J. F. A., Powell, R., Holland, T. J. B., & Palin, R. M.  
857 (2016). Activity–composition relations for the calculation of partial melting equilibria in  
858 metabasic rocks. *Journal of metamorphic Geology*, 34(9), 845-869.

859 Harley, S. L., Kelly, N. M., & Möller, A. (2007). Zircon behaviour and the thermal histories  
860 of mountain chains. *Elements*, 3(1), 25-30.

861 Holland, T. J. B., & Powell, R. (2011). An improved and extended internally consistent  
862 thermodynamic dataset for phases of petrological interest, involving a new equation of  
863 state for solids. *Journal of metamorphic Geology*, 29(3), 333-383.

864 Hynes, A., & Rivers, T. (2010). Protracted continental collision—evidence from the Grenville  
865 Orogen This article is one of a series of papers published in this Special Issue on the theme  
866 Lithoprobe—parameters, processes, and the evolution of a continent. *Canadian Journal of*  
867 *Earth Sciences*, 47(5), 591-620.

868 Indares, A. (1993). Eclogitized gabbros from the eastern Grenville Province: textures,  
869 metamorphic context, and implications. *Canadian Journal of Earth Sciences*, 30(1), 159-  
870 173.

871 Indares, A. (1997). Garnet-kyanite clinopyroxenites and garnet-kyanite restites from the  
872 Manicouagan imbricate zone; a case of high-P--high-T metamorphism in the Grenville  
873 Province. *The Canadian Mineralogist*, 35(5), 1161-1171.

874 Indares, A. D. (2003). Metamorphic textures and P–T evolution of high-P granulites from the  
875 Lelukuau terrane, NE Grenville Province. *Journal of Metamorphic Geology*, 21(1), 35-48.

876 Indares, A. (2020). Deciphering the metamorphic architecture and magmatic patterns of large  
877 hot orogens: Insights from the central Grenville Province. *Gondwana Research*, 80, 385-  
878 409.

879 Indares, A., & Dunning, G. (2001). Partial melting of high-P–T metapelites from the  
880 Tshenukutish Terrane (Grenville Province): petrography and U–Pb geochronology.  
881 *Journal of Petrology*, 42(8), 1547-1565.

882 Indares, A., & Dunning, G. (2004). Crustal architecture above the high-pressure belt of the  
883 Grenville Province in the Manicouagan area: new structural, petrologic and U–Pb age  
884 constraints. *Precambrian Research*, 130(1-4), 199-228.

885 Indares, A., & Dunning, G. (2018). Metamorphic Evolution of the central Grenville Province  
886 (Manicouagan area): a review. *Government of Quebec Report MM2017-01*, 20.

887 Indares, A., Dunning, G., & Cox, R. (2000). Tectono-thermal evolution of deep crust in a  
888 Mesoproterozoic continental collision setting: the Manicouagan example. *Canadian*  
889 *Journal of Earth Sciences*, 37(2-3), 325-340.

890 Indares, A., Dunning, G., Cox, R., Gale, D., & Connelly, J. (1998). High-pressure, high-  
891 temperature rocks from the base of thick continental crust: Geology and age constraints

892 from the Manicouagan Imbricate Zone, eastern Grenville Province. *Tectonics*, 17(3), 426-  
893 440.

894 Indares, A. & Rivers, T. (1995). Textures, metamorphic reactions and thermobarometry of  
895 eclogitized metagabbros: a Proterozoic example. *European Journal of Mineralogy*, 7, 43–56.

896 Indares, A., White, R. W., & Powell, R. (2008). Phase equilibria modelling of kyanite-bearing  
897 anatectic paragneisses from the central Grenville Province. *Journal of Metamorphic  
898 Geology*, 26(8), 815-836.

899 Jamieson, R. A., Beaumont, C., Nguyen, M. H., & Culshaw, N. G. (2007). Synconvergent  
900 ductile flow in variable-strength continental crust: Numerical models with application to  
901 the western Grenville orogen. *Tectonics*, 26(5).

902 Jamieson, R. A., Beaumont, C., Warren, C. J., & Nguyen, M. H. (2010). The Grenville  
903 Orogen explained? Applications and limitations of integrating numerical models with  
904 geological and geophysical data. *Canadian Journal of Earth Sciences*, 47(4), 517-539.

905 Jannin, S., Gervais, F., Moukhsil, A., Augland, L.E., & Crowley, J.L., (2018a). Déformations  
906 tardi-grenvilliennes dans la Ceinture parautochtone (Province de Grenville centrale):  
907 contraintes géochronologiques par couplage de méthodes U/Pb de haute résolution spatiale  
908 et de haute précision. *Canadian Journal of Earth Sciences*, 55, 406–435.

909 Jannin, S., Gervais, F., Moukhsil, A., & Augland, L. E. (2018b). Late-Grenvillian channel  
910 flow in the central Grenville Province (Manicouagan Reservoir area): New constraints  
911 from a structural and geochronological study of the Allochthon Boundary Thrust. *Journal  
912 of Structural Geology*, 115, 132-151.

913 Jeon, H., & Whitehouse, M. J. (2015). A critical evaluation of U–Pb calibration schemes used  
914 in SIMS zircon geochronology. *Geostandards and Geoanalytical Research*, 39(4), 443-  
915 452.

916 Johnson, T. A., Vervoort, J. D., Ramsey, M. J., Aleinikoff, J. N., & Southworth, S. (2018).  
917 Constraints on the timing and duration of orogenic events by combined Lu–Hf and Sm–Nd  
918 geochronology: an example from the Grenville orogeny. *Earth and Planetary Science*  
919 *Letters*, *501*, 152-164.

920 Johnson, T. A., Vervoort, J. D., Ramsey, M. J., Southworth, S., & Mulcahy, S. R. (2020).  
921 Tectonic evolution of the Grenville Orogen in the central Appalachians. *Precambrian*  
922 *Research*, *346*, 105740.

923 Jordan, S. L., Indares, A., & Dunning, G. (2006). Partial melting of metapelites in the Gagnon  
924 terrane below the high-pressure belt in the Manicouagan area (Grenville Province):  
925 pressure–temperature (P–T) and U–Pb age constraints and implications. *Canadian Journal*  
926 *of Earth Sciences*, *43*(9), 1309-1329.

927 Kendrick, J., & Indares, A. (2018). The reaction history of kyanite in high-P aluminous  
928 granulites. *Journal of Metamorphic Geology*, *36*(2), 125-146.

929 Kylander-Clark, A. R., Hacker, B. R., & Mattinson, C. G. (2012). Size and exhumation rate of  
930 ultrahigh-pressure terranes linked to orogenic stage. *Earth and Planetary Science Letters*,  
931 *321*, 115-120.

932 Kohn, M. J., Corrie, S. L., & Markley, C. (2015). The fall and rise of metamorphic zircon.  
933 *American Mineralogist*, *100*(4), 897-908.

934 Kohn, M. J., Engi, M., & Lanari, P. (2017). Petrochronology. *Methods and Applications*,  
935 *Mineralogical Society of America Reviews in Mineralogy and Geochemistry*, *83*, 575.

936 Lasalle, S., & Indares, A. (2014). Anatectic record and contrasting P–T paths of aluminous  
937 gneisses from the central Grenville Province. *Journal of Metamorphic Geology*, *32*(6),  
938 627-646.

939 Lasalle, S., Dunning, G., & Indares, A. (2014). *In situ* LA–ICP–MS dating of monazite from  
940 aluminous gneisses: insights on the tectono-metamorphic history of a granulite-facies

941 domain in the central Grenville Province. *Canadian Journal of Earth Sciences*, 51(6), 558-  
942 572.

943 Li, X. M., Cheng, H., Dragovic, B., Du, K. Y., & Zhou, Y. (2022). Multi-mineral  
944 petrochronology on a high-pressure mafic granulite reveals short-lived high-temperature  
945 metamorphism in the North China Craton. *Journal of Metamorphic Geology*.

946 Lotout, C., Pitra, P., Poujol, M., Anczkiewicz, R., & Van Den Driessche, J. (2018). Timing  
947 and duration of Variscan high-pressure metamorphism in the French Massif Central: A  
948 multimethod geochronological study from the Najac Massif. *Lithos*, 308, 381-394.

949 Lotout, C., Poujol, M., Pitra, P., Anczkiewicz, R., & Van Den Driessche, J. (2020). From  
950 burial to exhumation: emplacement and metamorphism of mafic eclogitic terranes  
951 constrained through multimethod petrochronology, case study from the Lévézou Massif  
952 (French Massif Central, Variscan Belt). *Journal of Petrology*, 61(4), ega046.

953 Lugmair, G. W., & Marti, K. (1978). Lunar initial  $^{143}\text{Nd}/^{144}\text{Nd}$ : differential evolution of the  
954 lunar crust and mantle. *Earth and Planetary Science Letters*, 39(3), 349-357.

955 Manzotti, P., Bosse, V., Pitra, P., Robyr, M., Schiavi, F., & Ballèvre, M. (2018). Exhumation  
956 rates in the Gran Paradiso Massif (Western Alps) constrained by in situ U–Th–Pb dating of  
957 accessory phases (monazite, allanite and xenotime). *Contributions to Mineralogy and  
958 Petrology*, 173, 1-28.

959 Marsh, J. H., & Culshaw, N. G. (2014). Timing and conditions of high-pressure  
960 metamorphism in the western Grenville Province: Constraints from accessory mineral  
961 composition and phase equilibrium modeling. *Lithos*, 200, 402-417.

962 Otamendi, J. E., de La Rosa, J. D., Douce, A. E. P., & Castro, A. (2002). Rayleigh  
963 fractionation of heavy rare earths and yttrium during metamorphic garnet growth. *Geology*,  
964 30(2), 159-162.

965 Pitra, P., Poujol, M., Van Den Driessche, J., Bretagne, E., Lotout, C., & Cogné, N. (2022).  
966 Late Variscan (315 Ma) subduction or deceptive zircon REE patterns and U–Pb dates from  
967 migmatite-hosted eclogites?(Montagne Noire, France). *Journal of Metamorphic Geology*,  
968 40(1), 39-65.

969 Rivers, T. (2008). Assembly and preservation of lower, mid, and upper orogenic crust in the  
970 Grenville Province—Implications for the evolution of large hot long-duration orogens.  
971 *Precambrian Research*, 167(3-4), 237-259.

972 Rivers, T. (2009). The Grenville Province as a large hot long-duration collisional orogen—  
973 insights from the spatial and thermal evolution of its orogenic fronts. *Geological Society*,  
974 *London, Special Publications*, 327(1), 405-444.

975 Rivers, T. (2012). Upper-crustal orogenic lid and mid-crustal core complexes: signature of a  
976 collapsed orogenic plateau in the hinterland of the Grenville Province. *Canadian Journal*  
977 *of Earth Sciences*, 49(1), 1-42.

978 Rivers, T., Culshaw, N., Hynes, A., Indares, A., Jamieson, R., Martignole, J., 2012. *The*  
979 *Grenville orogen – a post Lithoprobe perspective*. In: Percival, J.A., Cook, F.A., Clowes,  
980 R.M. (Eds.), *Tectonic Styles in Canada: The Lithoprobe Perspective*. Geological Survey of  
981 *Canada*, Special Paper 49, pp. 97–236.

982 Rivers, T., Ketchum J., Indares A. & Hynes, A. (2002). The high pressure belt in the  
983 Grenville Province: architecture, timing, and exhumation. *Canadian Journal of Earth*  
984 *Sciences*, 39, 867–893.

985 Roberts, N. M., Salminen, J., Johansson, Å., Mitchell, R. N., Palin, R. M., Condie, K. C., &  
986 Spencer, C. J. (2022). On the enigmatic mid-Proterozoic: Single-lid versus plate tectonics.  
987 *Earth and Planetary Science Letters*, 594, 117749.

988 Rubatto, D. (2002). Zircon trace element geochemistry: partitioning with garnet and the link  
989 between U–Pb ages and metamorphism. *Chemical geology*, 184(1-2), 123-138.

- 990 Rubatto, D. (2017). Zircon: the metamorphic mineral. *Reviews in mineralogy and*  
991 *geochemistry*, 83(1), 261-295.
- 992 Scherer, E. E., Cameron, K. L., & Blichert-Toft, J. (2000). Lu–Hf garnet geochronology:  
993 closure temperature relative to the Sm–Nd system and the effects of trace mineral  
994 inclusions. *Geochimica et Cosmochimica Acta*, 64(19), 3413-3432.
- 995 Smit, M. A., Scherer, E. E., & Mezger, K. (2013). Lu–Hf and Sm–Nd garnet geochronology:  
996 chronometric closure and implications for dating petrological processes. *Earth and*  
997 *Planetary Science Letters*, 381, 222-233.
- 998 Söderlund, U., Patchett, P. J., Vervoort, J. D., & Isachsen, C. E. (2004). The  $^{176}\text{Lu}$  decay  
999 constant determined by Lu–Hf and U–Pb isotope systematics of Precambrian mafic  
1000 intrusions. *Earth and Planetary Science Letters*, 219(3-4), 311-324.
- 1001 Spencer, C. J., Mitchell, R. N., & Brown, M. (2021). Enigmatic Mid-Proterozoic Orogens:  
1002 Hot, Thin, and Low. *Geophysical Research Letters*, 48, e2021GL093312.
- 1003 Sun, S. S., & McDonough, W. F. (1989). Chemical and isotopic systematics of oceanic  
1004 basalts: implications for mantle composition and processes. *Geological Society, London,*  
1005 *Special Publications*, 42(1), 313-345.
- 1006 Štípská, P., Powell, R., Hacker, B. R., Holder, R., & Kylander-Clark, A. R. C. (2016).  
1007 Uncoupled U/Pb and REE response in zircon during the transformation of eclogite to mafic  
1008 and intermediate granulite (Blanský les, Bohemian Massif). *Journal of Metamorphic*  
1009 *Geology*, 34(6), 551-572.
- 1010 Tang, M., Erdman, M., Eldridge, G., & Lee, C. T. A. (2018). The redox “filter” beneath  
1011 magmatic orogens and the formation of continental crust. *Science Advances*, 4(5),  
1012 eaar4444.
- 1013 Tang, M., Chu, X., Hao, J., & Shen, B. (2021). Orogenic quiescence in Earth’s middle age.  
1014 *Science*, 371(6530), 728-731.

1015 Taylor, R. J., Kirkland, C. L., & Clark, C. (2016). Accessories after the facts: Constraining the  
1016 timing, duration and conditions of high-temperature metamorphic processes. *Lithos*, 264,  
1017 239-257.

1018 Tilhac, R., Hidas, K., Oliveira, B., & Garrido, C. J. (2023). Evidence of ghost plagioclase  
1019 signature induced by kinetic fractionation of europium in the Earth's mantle. *Nature*  
1020 *Communications*, 14(1), 1099.

1021 Touret, J.L.R., Nijland, T.G., 2013. Prograde, peak and retrograde metamorphic fluids  
1022 and associated metasomatism in upper amphibolite to granulite facies transition zones, in:  
1023 Harlov, D.E., Austerheim, H. (Eds.), *Metasomatism and the Chemical Transformation of*  
1024 *Rock*. Springer, Berlin, Heidelberg, pp. 415-469.

1025 Tual, L., Smit, M. A., Cutts, J., Kooijman, E., Kielman-Schmitt, M., Majka, J., & Foulds, I.  
1026 (2022). Rapid, paced metamorphism of blueschists (Syros, Greece) from laser-based zoned  
1027 Lu-Hf garnet chronology and LA-ICPMS trace element mapping. *Chemical Geology*, 607,  
1028 121003.

1029 Wang, J. M., Wu, F. Y., Rubatto, D., Liu, S. R., Zhang, J. J., Liu, X. C., & Yang, L. (2017).  
1030 Monazite behaviour during isothermal decompression in pelitic granulites: a case study  
1031 from Dinggye, Tibetan Himalaya. *Contributions to Mineralogy and Petrology*, 172(10), 1-  
1032 30.

1033 Wang, D., Vervoort, J. D., Fisher, C. M., Cao, H., & Li, G. (2019). Integrated garnet and  
1034 zircon-titanite geochronology constrains the evolution of ultra-high-pressure terranes: An  
1035 example from the Sulu orogen. *Journal of Metamorphic Geology*, 37(5), 611-631.

1036 Warren, C. J. (2013). Exhumation of (ultra-) high-pressure terranes: concepts and  
1037 mechanisms. *Solid Earth*, 4(1), 75-92.

- 1038 Whitehouse, M. J., & Platt, J. P. (2003). Dating high-grade metamorphism—constraints from  
1039 rare-earth elements in zircon and garnet. *Contributions to Mineralogy and Petrology*,  
1040 *145*(1), 61-74.
- 1041 Whitehouse, M. J., Ravindra Kumar, G. R., & Rimša, A. (2014). Behaviour of radiogenic Pb  
1042 in zircon during ultrahigh-temperature metamorphism: an ion imaging and ion tomography  
1043 case study from the Kerala Khondalite Belt, southern India. *Contributions to Mineralogy  
1044 and Petrology*, *168*(2), 1-18.
- 1045 Yakymchuk, C., & Brown, M. (2014). Behaviour of zircon and monazite during crustal  
1046 melting. *Journal of the Geological Society*, *171*(4), 465-479.
- 1047 Yang, P., & Indares, A. D. (2005). Mineral zoning, phase relations, and P–T evolution of  
1048 high-pressure granulites from the Lelukuau terrane, northeastern Grenville Province,  
1049 Quebec. *The Canadian Mineralogist*, *43*(1), 443-462.
- 1050

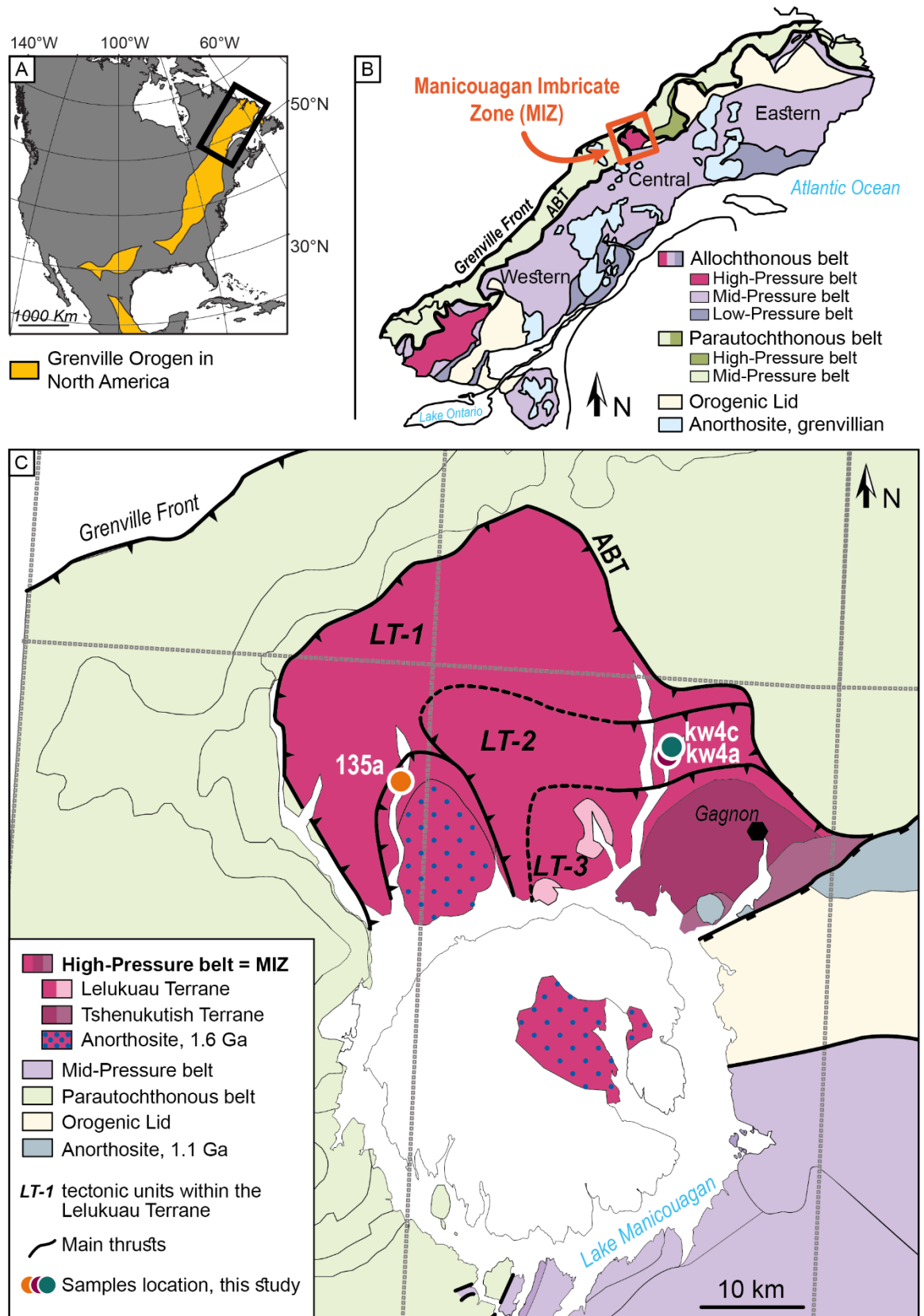


Figure 1

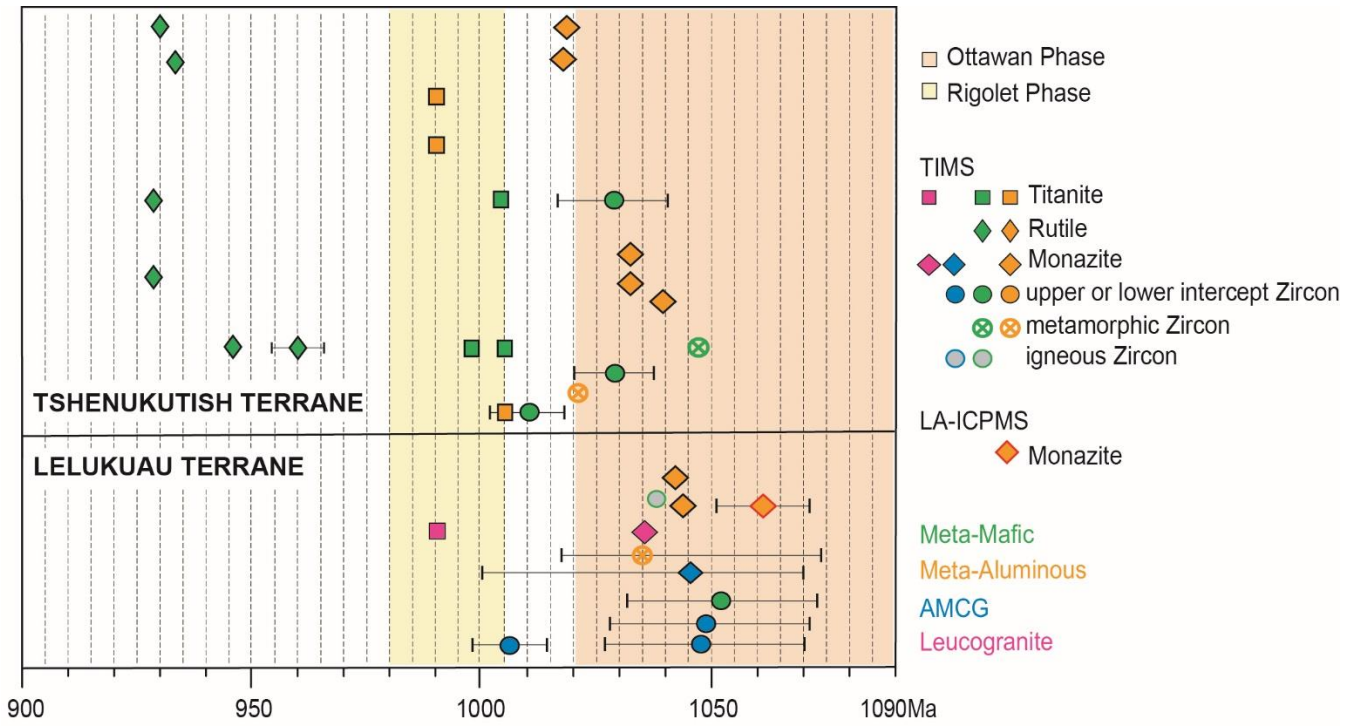


Figure 2

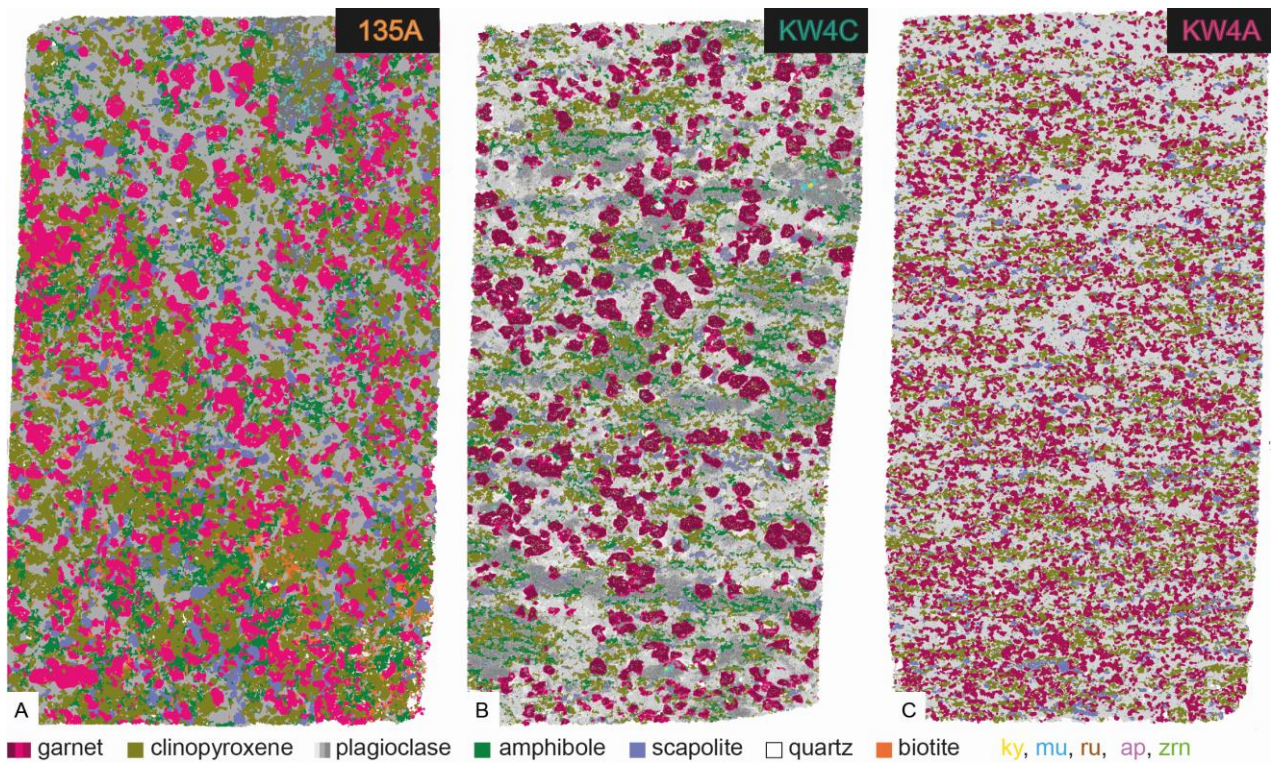


Figure 3

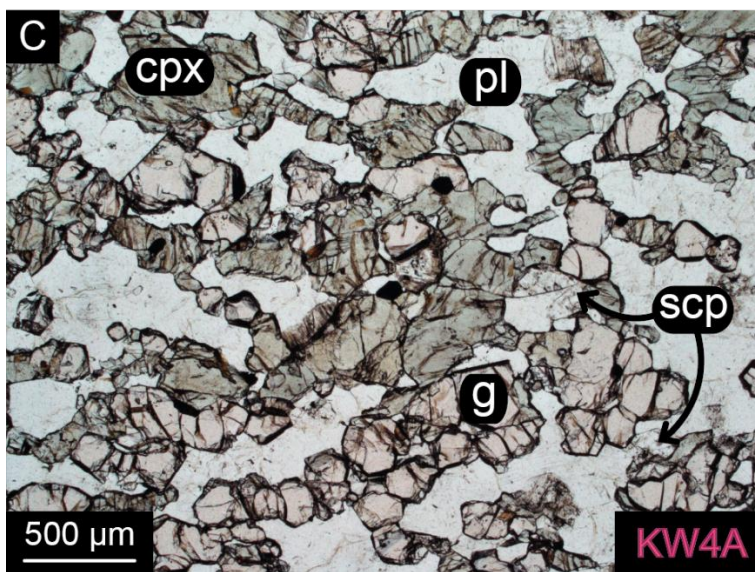
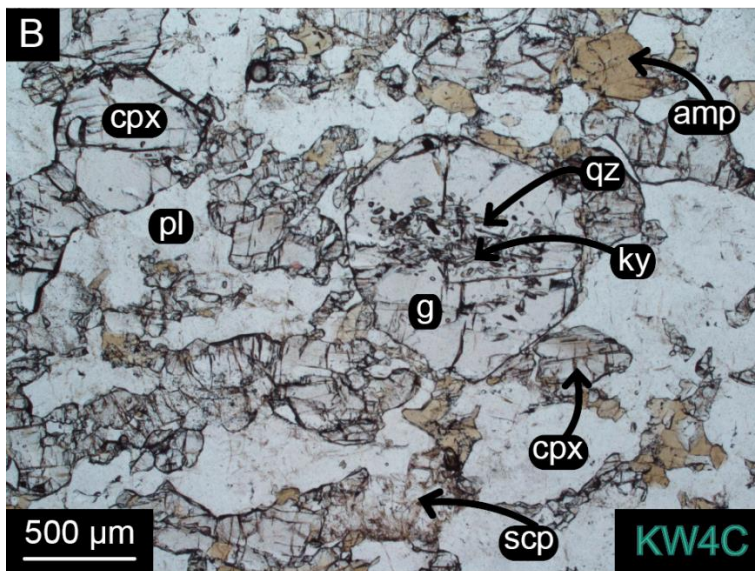
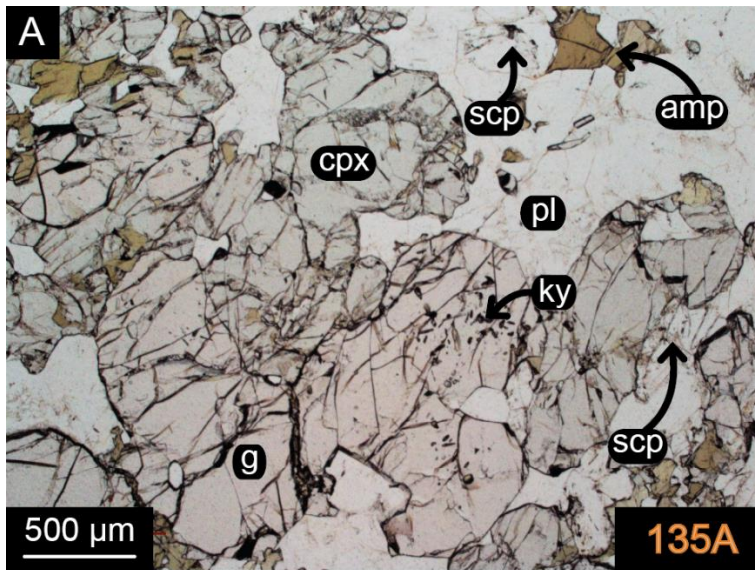


Figure 4

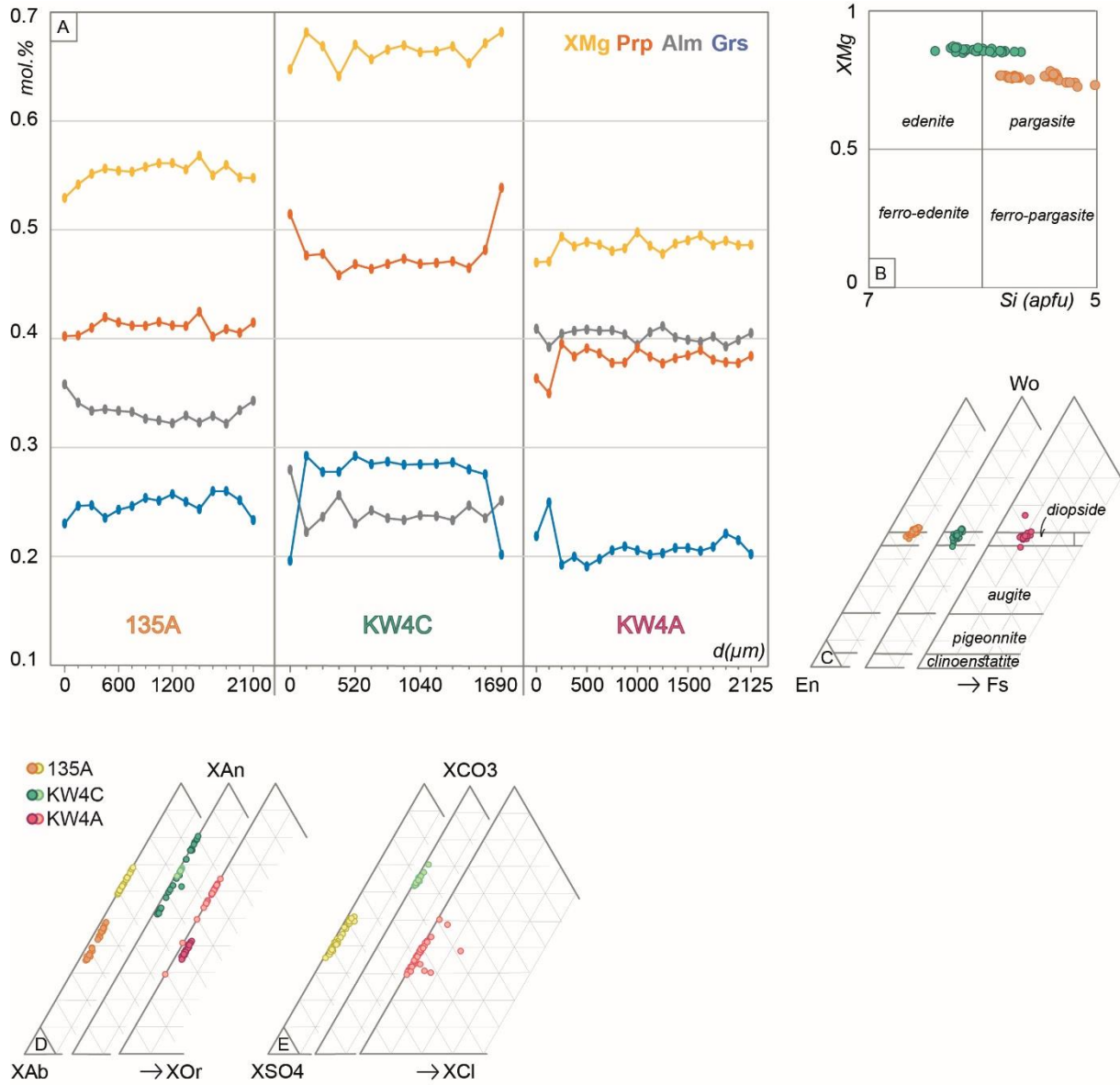
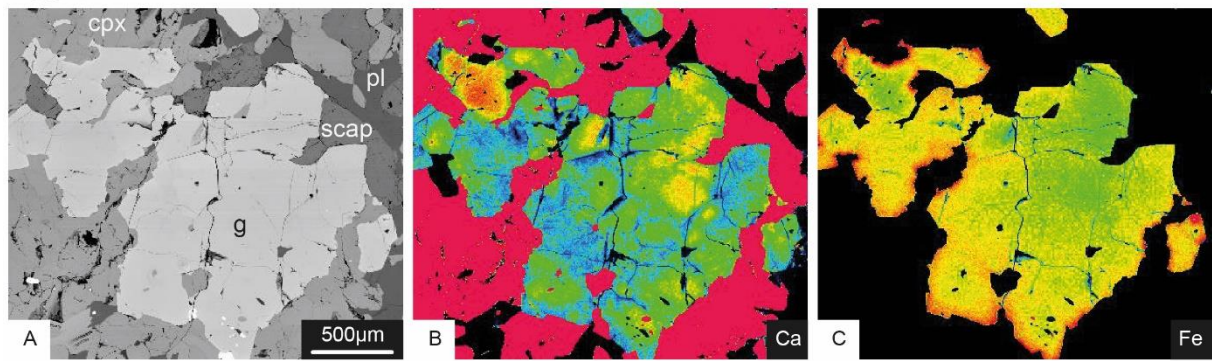
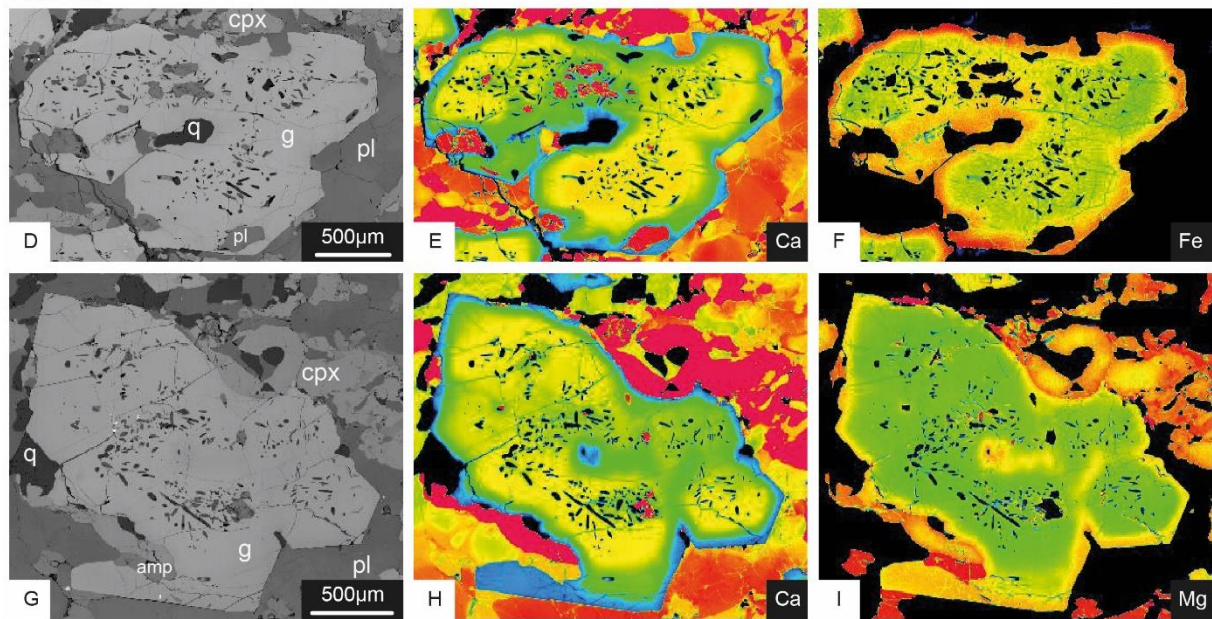


Figure 5

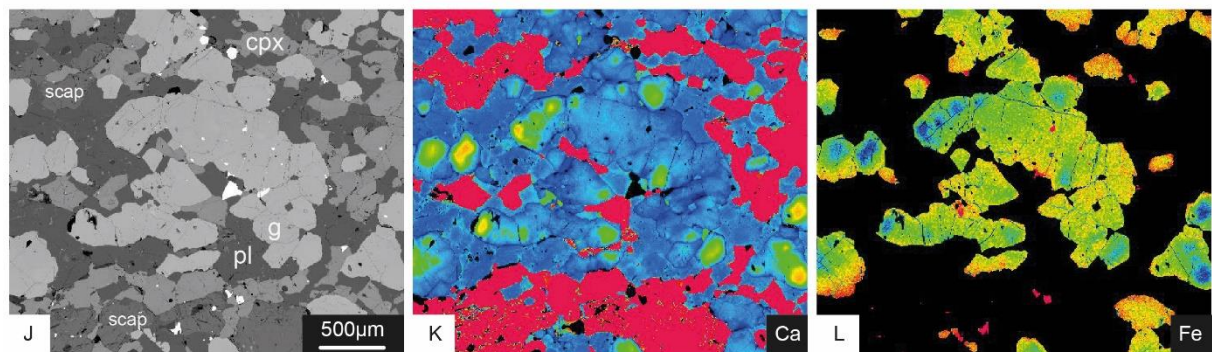
135A



KW4C



KW4A



\*Figure 6

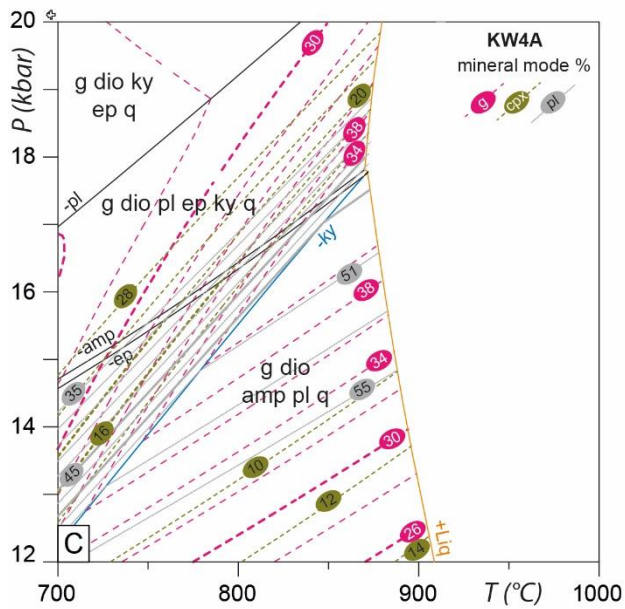
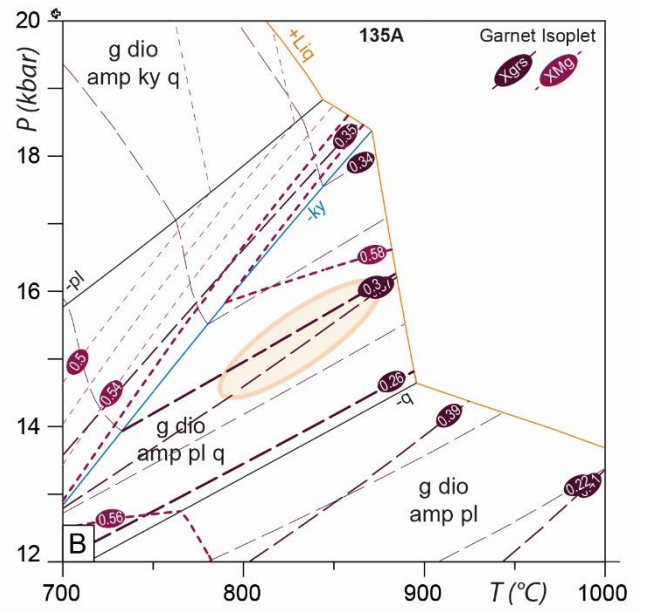
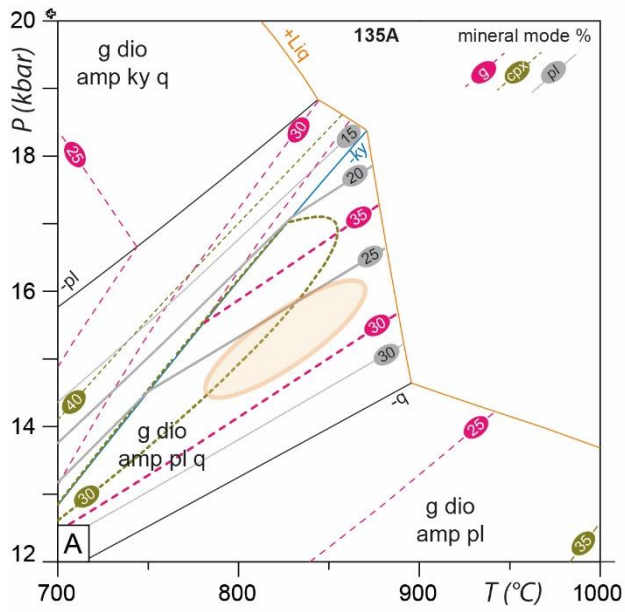


Figure 7

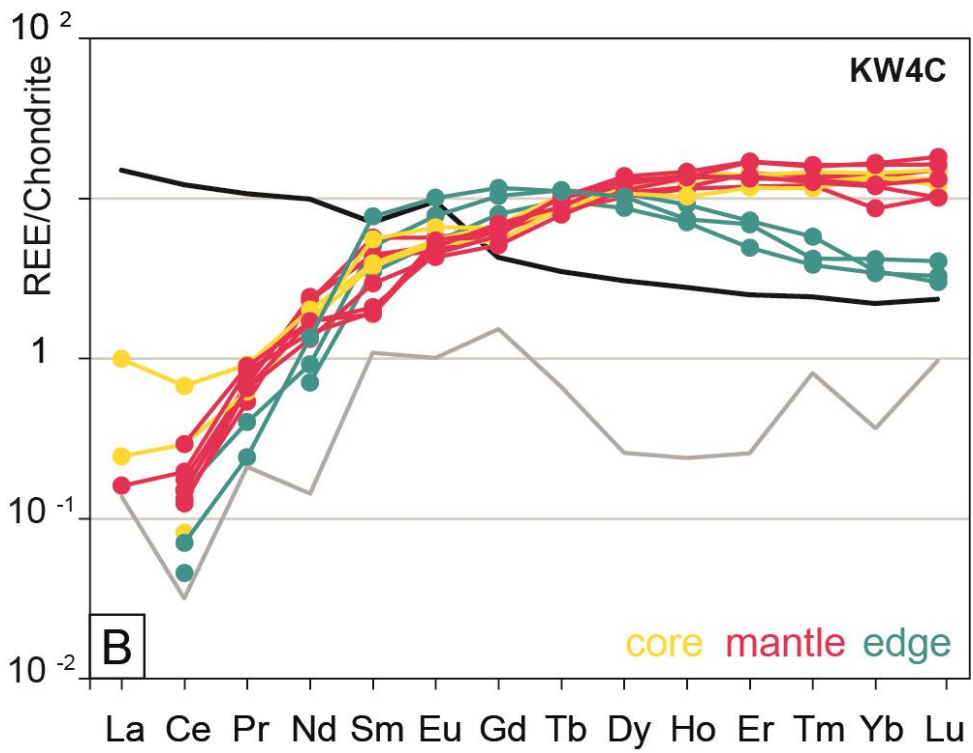
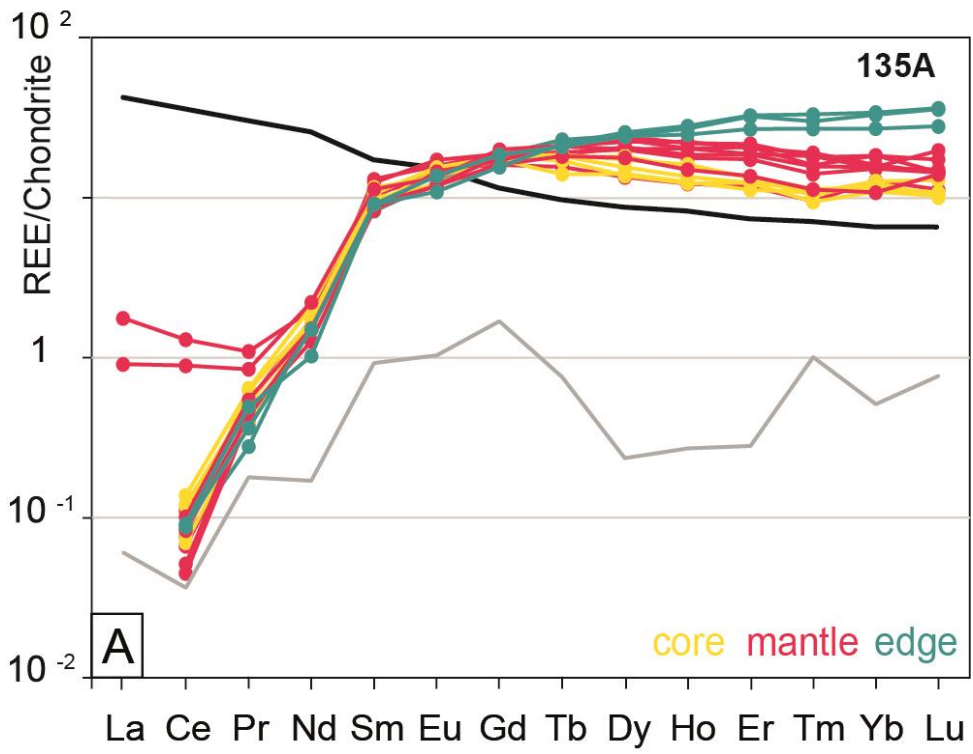


Figure 8

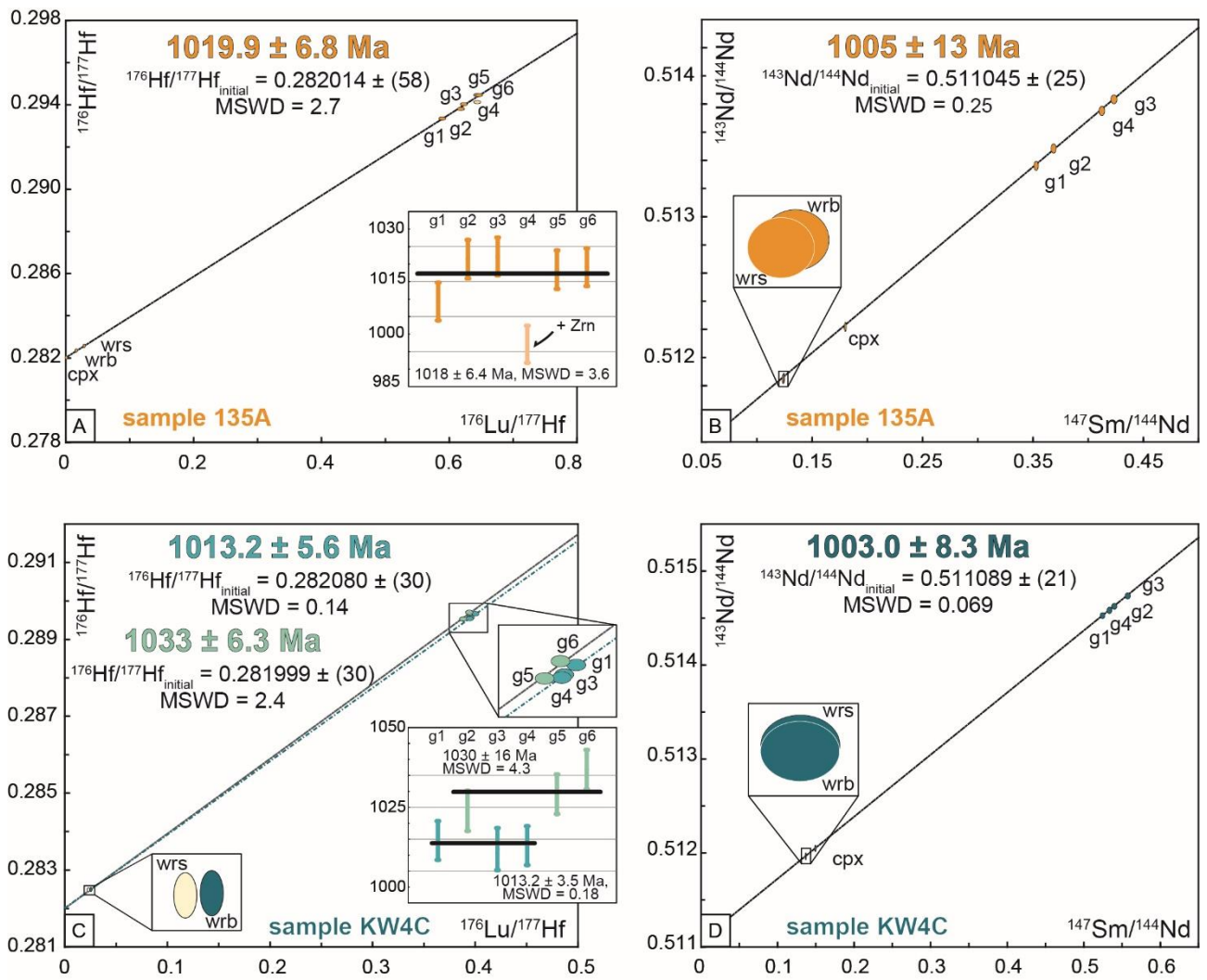


Figure 9

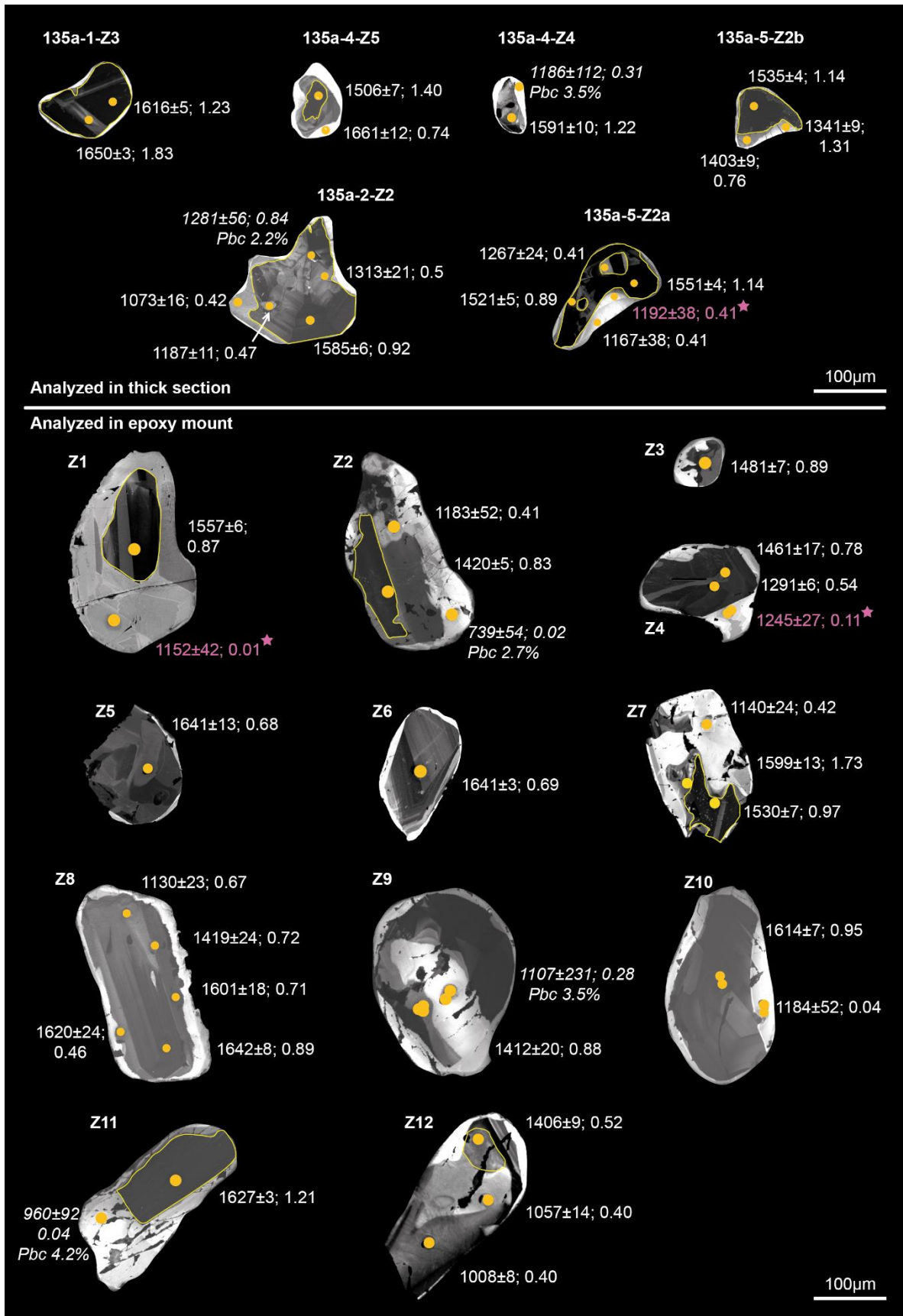


Figure 10

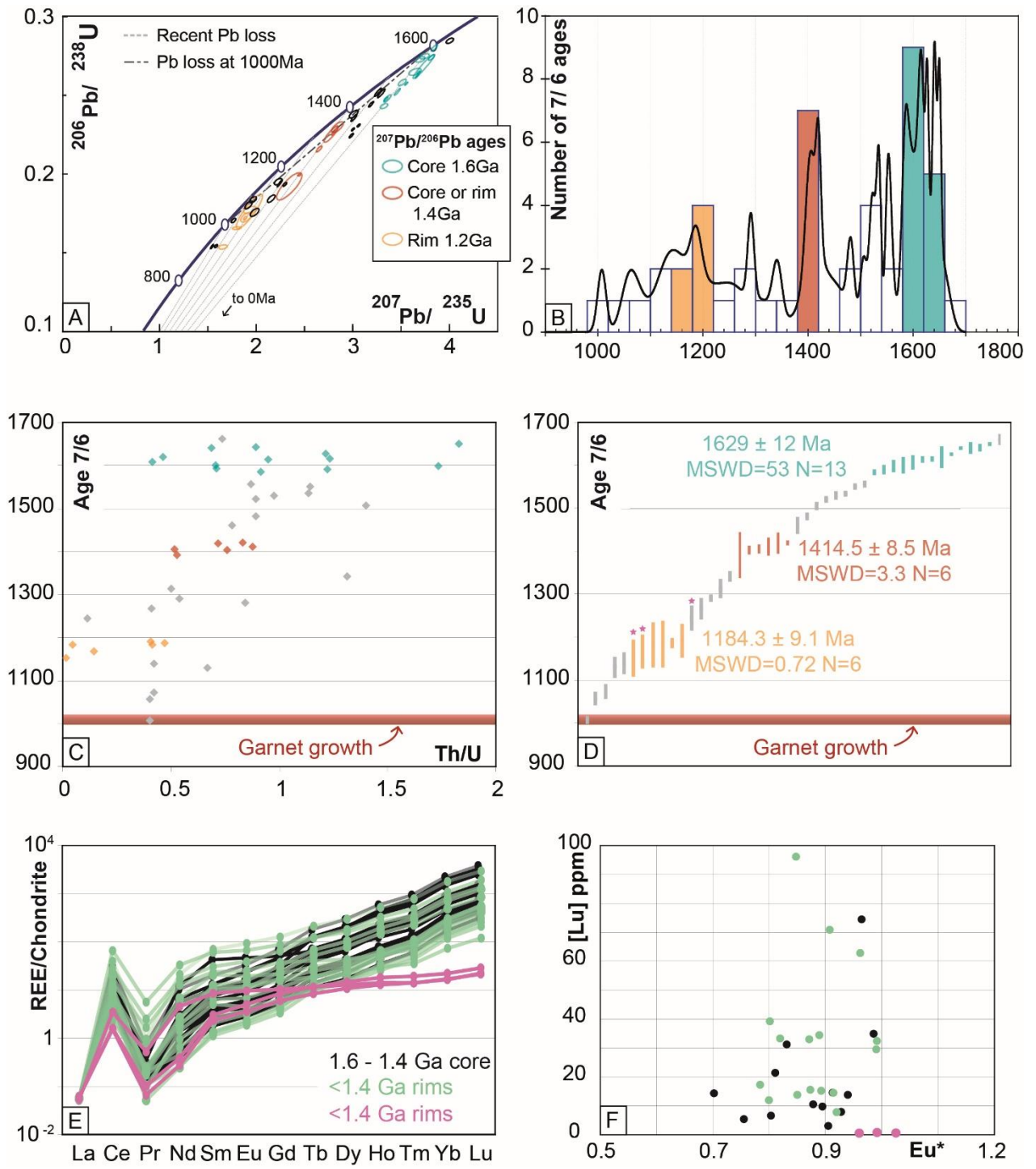


Figure 11

Table 1

	<b>garnet</b>	<b>clinopyroxene</b>	<b>plagioclase</b>	<b>amphibole</b>	<b>scapolite</b>	<b>quartz</b>	<b>biotite</b>
<b>135A</b>	30	30	22	10	5	<0.5	1.5
<b>KW4C</b>	21	14	50	8	2.5	4.5	<0.5
<b>KW4A</b>	47	28	17	<0.5	5	<0.5	<0.5

Sample <sup>a</sup>	Lu <sup>b</sup> (ppm)	Hf <sup>b</sup> (ppm)	<sup>176</sup> Lu/ <sup>177</sup> Hf <sup>c</sup>	<sup>176</sup> Hf/ <sup>177</sup> Hf	± <sup>d</sup>	2-point date (Ma) <sup>e</sup>	Sm <sup>b</sup> (ppm)	Nd <sup>b</sup> (ppm)	<sup>147</sup> Sm/ <sup>144</sup> Nd <sup>c</sup>	<sup>143</sup> Nd/ <sup>144</sup> Nd	± <sup>d</sup>	2-point date (Ma) <sup>e</sup>
<b>135A</b>												
g1	0.582	0.134	0.6187	0.293805	31	1009.3 ± 6.2	1.60	2.74	0.3526	0.513367	27	999 ± 26
g2	0.594	0.136	0.6234	0.294034	31	1021.4 ± 6.2	1.59	2.61	0.3692	0.513492	27	1010 ± 24
g3	0.600	0.132	0.6448	0.294456	31	1022.2 ± 6.1	1.54	2.19	0.4237	0.513839	27	1003 ± 20
g4	0.601	0.133	0.6433	0.294129	31	997.1 ± 6.0	1.56	2.29	0.4124	0.513757	27	998 ± 21
g5	0.583	0.140	0.5895	0.293350	31	1018.4 ± 6.3	*	*	*	*	*	*
g6	0.589	0.130	0.6466	0.294454	29	1019.1 ± 6.1	*	*	*	*	*	*
cpx	0.014	1.96	0.0010	0.282014	28		2.54	8.57	0.1791	0.512222	27	
wrs	0.160	0.783	0.0290	0.282572	28		1.11	5.45	0.1229	0.511853	27	
wrb	0.419	3.59	0.0166	0.282351	28		2.74	13.5	0.1232	0.511862	26	
<b>KW4C</b>												
g1	0.219	0.078	0.4002	0.289660	31	1014.6 ± 7.8	0.733	0.847	0.5232	0.514536	27	1006 ± 16
g2	0.217	0.077	0.4012	0.289747	32	1023.9 ± 7.9	0.702	0.789	0.5385	0.514635	27	1006 ± 15
g3	0.216	0.078	0.3956	0.289554	35	1011.9 ± 6.6	0.711	0.774	0.5563	0.514744	27	1002 ± 15
g4	0.221	0.079	0.3948	0.289546	30	1013 ± 7.8	0.754	0.856	0.5325	0.514593	27	1004 ± 16
g5	0.214	0.078	0.3879	0.289527	30	1029.1 ± 7.9	*	*	*	*	*	*
g6	0.205	0.074	0.3940	0.289699	30	1036.8 ± 7.9	*	*	*	*	*	*
cpx	0.006	1.15	0.0008	0.281973	28		5.44	22.4	0.1466	0.512056	27	
wrs	0.055	0.342	0.0228	0.282495	29		1.08	4.88	0.1343	0.511975	27	
wrb	0.057	0.321	0.0251	0.282488	28		1.09	4.93	0.1343	0.511968	26	

Table 2